Master's thesis

NTNU
Norwegian University of Science and Technology
Faculty of Natural Sciences
Department of Chemical Engineering

Alicia San Martin Rueda

In-situ potassium poisoning on cobalt-based catalysts for Fischer-Tropsch synthesis

Master's thesis in Chemical Engineering and Biotechnology
Supervisor: Edd Anders Blekkan
Co-supervisor: Oscar Luis Ivanez Encinas
June 2023

NTNU
Norwegian University of
Science and Technology

Alicia San Martin Rueda

In-situ potassium poisoning on cobalt-based catalysts for Fischer-Tropsch synthesis

Master's thesis in Chemical Engineering and Biotechnology
Supervisor: Edd Anders Blekkan
Co-supervisor: Oscar Luis Ivanez Encinas
June 2023

Norwegian University of Science and Technology
Faculty of Natural Sciences
Department of Chemical Engineering

NTNU
Norwegian University of
Science and Technology

Preface

This thesis is a fulfilment of the course “TKP4901-Chemical Process Technology, Master’s Thesis”, and was written in the Catalysis Group in the Department of Chemical Engineering at the Norwegian University of Science and Technology.

I will be forever grateful to Edd for giving me the opportunity to take part in the catalysis group and for always being concern about my continued progress. I would especially like to thank Oscar for his immeasurable assistance throughout the entire year and for all I have learnt with this project while working close to him. And of course, Estelle, for her tremendous generosity and her constant willingness to offer me her help whenever I needed it.

Finally, I would like to thank everyone who accompanied me during my exchange and made it the best experience of my life, especially Carlos and Ahmed for the innumerable coffees and chats at Anacleta's, I deeply love you. And my family, who are always by my side wherever I go.

Declaration of Compliance

I, Alicia San Martín Rueda, declare that this is an independent work according to the exam regulations of the Norwegian University of Science and Technology.

Trondheim, Norway 15.06.2023

Alicia San Martin Rueda

Alicia San Martín Rueda

Abstract

Nowadays it is a fact that the energy demand is rising, and it is expected to continue. Furthermore, the world is experiencing now an energy crisis, both economic and environmental. Therefore, replacing fossil fuels with alternative energy sources is crucial, which is why biofuels derived from biomass are gaining popularity. For this purpose, the Fischer-Tropsch synthesis over cobalt-based catalysts seems to be promising. Fischer Tropsch is part of The Biomass to Liquid Process. Among the different products, light olefins represent added value compared to fuels, which always will be the main product. Via gasification, the biomass is converted to syngas that can be transformed into liquid hydrocarbons via Fischer-Tropsch. However, the gasification leads to the appearance of numerous impurities. Cleaning this syngas is essential since these impurities can be a poison for the catalysts, leading consequently to their early deactivation. This cleaning process is very expensive, so it is really important to evaluate the potential poisons in order to make it economically viable. Among these impurities, potassium is an essential alkali metal present in most biomass feedstocks. Its behaviour and effect in cobalt-based catalysts has been extensively studied but research over this topic is still uncertain.

In this project a study has been carried out on 4 cobalt-based catalysts, promoted by Mn and Re and supported on alumina, titania, and silica. They have been poisoned in-situ with different K-salts: KNO_3, KCl and K_2SO_4. This work has reaffirmed previous research that claimed that potassium causes a drop in catalyst activity and selectivity towards methane, while favouring C_{5+} products. KNO_3 seems to be the K-salt that most influences catalyst behaviour, probably due to the occurrence of side reactions. At high potassium concentrations it is possible that the active sites of the precursor metal are blocked, so the effects on activity and selectivity are irreversible and further addition of K has no major effect. Moreover, the use of different support materials may influence the activity behaviour, probably due to the influence of the particle size. Also, it seems that the different cobalt loading does not make the potassium act differently on the catalyst. However, still further work will be necessary to fully understand the impact of this impurity over cobalt-based catalysts.

Table of Contents

List of Figures

List of Tables

List of Symbols

i	Number of carbon atoms (hydrocarbon chain length)
w_i	Weight fraction of a chain length i
α	Chain growth probability
V	Volume
V_m	Monolayer volume
P	Partial pressure
P_0	Saturation pressure
C	BET constant
S_{BET}	BET Surface Area
N_A	Avogadro number
A_x	Cross-sectional area
v	Molar volume
γ	Surface tension
r_K	Kelvin radius
R	Ideal gas constant
T	Temperature
D_{chem}	Dispersion obtained by chemisorption
F_s	Stoichiometry factor
N_T	Total number of metal atoms
d_p	Particle size obtained by chemisorption

n_r	Order of reflection
λ	X-Ray wavelength
d	Distance between lattice planes
θ	Angle between the sample surface rays and the normal direction
L	Length of the particles
β	Peak width
d_c	Metallic crystal size measured by XRD
τ	Crystallite size
D_{XRD}	Dispersion obtained by XRD
ΔG	Gibbs free energy
ΔG°	Standard Gibbs energy
x_{CO}	CO conversion
F_{CO}	CO molar flow
$F_{CO,0}$	CO initial molar flow
r	Reaction rate
M_m	Molecular weight
x_m	Weight fraction of the metal
m	Weight
S_B	Selectivity towards the desirable product B
F	Molecular mass factor

List of Abbreviations

BtL	Biomass to Liquid
FTS	Fischer Tropsch Synthesis
FT	Fischer-Tropsch
PM	Particulate Matter
SC	Steam Cracking
WGS	Water Gas Shift
LHHW	Langmuir-Hinshelwood-Hougen-Watson
ASF	Anderson Schulz Flory
P/O	Paraffin/Olefin Ratio
IWI	Incipient Wetness Impregnation
BET	Brunauer Emmett Teller
BJH	Barret, Joyner and Halenda
XRD	X-Ray Diffraction
TPR	Temperature Programmed Reduction
XRF	X-Ray Fluorescence
STEM	Scanning Transmission Electron Microscopy
EDX	Energy Dispersive X-Ray
TOF	Turnover Frequency
STY	Site Time Yield
GC	Gas Chromatograph

TCD Thermal Conductivity Detector

FID Flame Ionization Detector

hoS Hours on Stream

ToS Time on Stream

1 Introduction

The specialization project accomplished in the previous semester [1] is continued in this master's thesis. It is for this reason that some parts in the introduction, theory and experimental methods are drawn from this earlier work.

1.1 Motivation and Background

Nowadays, it is a fact that there is a serious global energy issue. Reasons such as the Covid-19 pandemic, the ongoing war conflict and the high demand for energy have caused a significant rise in its price. Moreover, not only the economic component but also the environmental one is affected. In particular, the oil industry currently faces major uncertainties in the short and long term. The use of fossil fuels is one of the main reasons for the global environmental crisis. They are the primary causes of global warming and climate change due to their production and release of CO_2 and other greenhouse gases into the atmosphere. In fact, CO_2 emissions from the burning of fossil fuels worldwide increased to a record level in 2021 [2]. Although a major improvement is foreseen in the near-term future, greater efforts are needed to find a long-term solution.

The vulnerability of the energy market serves as a reminder of the fragility and inadequate sustainability of the current energy system. Therefore, replacing fossil fuels with alternative energy sources is crucial. In recent years, the production of biofuels from biomass has gained considerable importance, as it can reduce these greenhouse gas emissions. Besides, biomass is a very abundant source, and it opens the possibility to use waste as a feedstock. Biomass to Liquid Process (BtL) converts biomass into clean, carbon-neutral biofuels [3]. Whitin this technology biomass gasification and Fischer-Tropsch Synthesis (FTS) is a very interesting alternative. The process involves the gasification of biomass into synthesis gas (syngas), composed mainly of H_2 and CO. The syngas is then converted into liquid hydrocarbons by the catalytic Fischer-Tropsch (FT) process. The Fischer-Tropsch Synthesis yields a wide variety of hydrocarbons, paraffins and olefins and is currently considered as one of the most competent technologies to produce biofuels [4].

The economic sustainability of the entire process is crucial. Increasing the process selectivity toward products with added value, such as light olefins, is one option for enhancing its profitability. Light olefins are recognized among the most used petrochemical feedstocks, employed as chemical intermediates in the manufacture of a variety of valuable products [5]. On the other hand, the biomass gasification process leads to the appearance of numerous impurities in the syngas [6]. Cleaning the synthesis gas is essential since these impurities can poison the catalysts, leading consequently to their early deactivation [4,7]. However, the cleaning process is very expensive, so it is vital to evaluate the potential poisons in order to make it economically feasible.

This is where the role of the catalysts becomes relevant. A catalyst that provides reasonable selectivity towards the product of interest, with high activity and ensuring a certain long-term stability can solve the problem of economic and commercial viability of BtL technology [8]. Numerous metal-based catalysts have been extensively studied, but it appears that cobalt is an interesting candidate due to its high activity at low temperature and selectivity to long chain hydrocarbons [9,10].

However, cobalt-based catalysts for FTS are particularly sensitive to impurities present in syngas. Specifically, potassium is an alkali metal present in most biomass feedstocks. Its behaviour and effect in cobalt-based catalysts has been extensively studied [11,12]. In most of the research, the deposition of K has been done via impregnation and other ex-situ techniques. However, little research has been done with in-situ contamination. Understanding the catalysts and its contaminants can lead to the improvement of the BtL technologies. In addition, evaluate the acceptable levels of impurities in the catalysts can reduce the costs in the syngas clean-up.

1.2 Main objective

The aim of this project was to study of the effect of potassium present in the syngas in the Fischer-Tropsch synthesis. For this purpose, 4 different cobalt-based catalysts, promoted by manganese and rhenium and, supported on different materials as alumina, titania, and silica have been poisoned and tested during the FTS.

The work includes the synthesis of the catalysts, their characterization and testing. Especially this work focuses on testing and characterization post-FTS. In order to test the in-situ contamination, several potassium solutions prepared from different potassium-salts were added during the reaction by means of a syringe pump. In this work, it has been studied the effect of the different K precursors and its concentration. In addition, the effect of the support and active metal loading were also tested. All catalysts were compared in terms of activity and selectivity before and after the contamination. Finally, the physical and chemical properties of all catalysts after FTS will be studied and compared with those before the reaction.

This will allow us to gain a deeper understanding of potassium behaviour in the Fischer-Tropsch synthesis and develop preventive measures against catalyst deactivation.

2 Theory

This chapter was partially influenced by earlier work [1], as this project is based on the same theoretical foundation.

2.1 Biomass to Liquid Process

Through a series of procedures, the Biomass to Liquid Process transforms a carbon-rich feedstock (biomass) into liquid fuels [13]. Via gasification, the biomass is converted to syngas that can be transformed into liquid hydrocarbons via Fischer-Tropsch.

Figure 2.1 shows an outline of the steps involved in the BtL process [3]. First, the biomass is gasified to obtain a synthesis gas (syngas), consisting mainly of a mixture of H_2 and CO and to a lesser extent CH_4 and CO_2. Along with these elements, many contaminants are released during gasification and must be eliminated by cleaning procedures. Furthermore, CO and H_2 are separated from the other components, as they are the main gases that will be involved in the FTS. After synthesis, the product must go through a series of conditioning and upgrading stages to end up with the desired characteristics and properties that allow its commercial use.

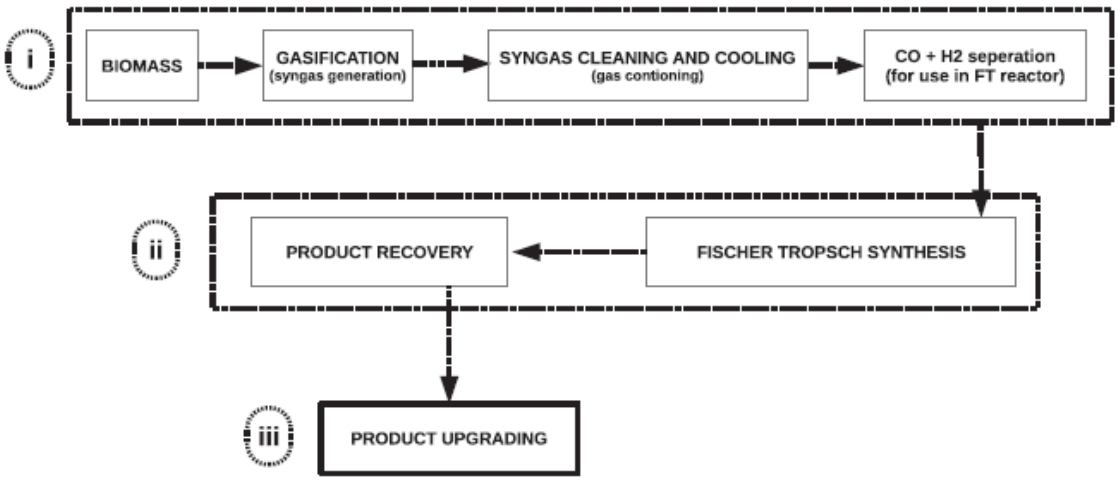

Figure 2.1. Biomass to Liquid Process: (i) Biomass gasification and syngas cleaning, (ii) Fischer-Tropsch synthesis (iii) Product upgrading [3]

2.1.1 Biomass conversion via gasification

Gasification consists of a thermochemical process that transforms biomass into a versatile gaseous mixture known as synthesis gas [14]. It takes place in the presence of a gasifying agent at temperatures above 700 °C. The syngas obtained consists mainly of CO, H_2, CO_2 and CH_4 and pollutants such as H_2O, alkali metals, H_2S, NH_3, tars and other trace species, whose compositions are dependent on the type of feedstock and gasification technology [14].

Figure 2.2 displays a general biomass gasification process. The feedstock is introduced into the bubbling bed reactor at temperatures of 800-900 °C and the char that was formed might be also placed in a combustion device to be burned, providing energy [15].

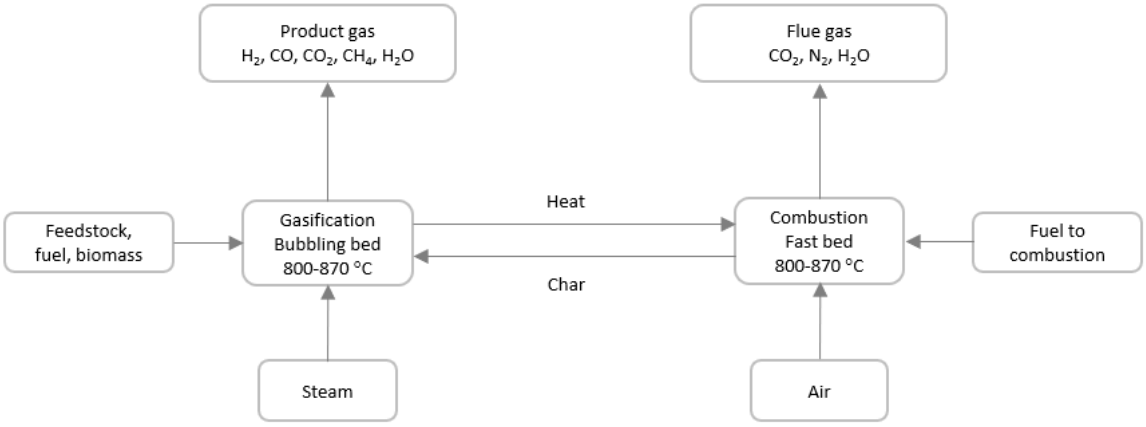

Figure 2.2. Steam gasification of biomass process [15]

2.1.2 Syngas cleaning

Cleaning of the obtained syngas is a crucial step in the BtL process. The released impurities can poison catalysts and induce early deactivation. Even more so for FTS, since catalysts are particularly vulnerable to even trace concentrations of these compounds [16]. Furthermore, this cleaning process is expensive, and therefore evaluating possible contaminants is crucial to make it economically viable.

Particulate matter (PM), condensable hydrocarbons (tars), alkaline metals (Na + K), nitrogen (NH_3 + HCN), sulphur (H_2S + COS + CS_2), and halides (HCl + HBr + HF) compounds are the different categories of pollutants found in syngas [14]. The synthesis gas requirements for the FT method are listed in the following Table 2.1.

Table 2.1. FT feed gas specifications [17]

Impurity	**Removal level**
$H_2S + COS + CS_2$	< 1 ppmV
$NH_3 + HCN$	< 1 ppmV
HCl + HBr + HF	< 10 ppbV
Solids (soot, dust, ash)	essentially completely
Organic compounds (tars)	below dew point
Alkaline metals	< 10 ppbV

Metal surfaces corrode due to sulphur compounds. Even small amounts of sulphur can eventually poison catalysts [6] and some studies reported its negative effect in the catalyst reducibility [18]. Ammonia concentration in syngas is typically limited between a few hundred and a few thousand parts per million. However, in certain circumstances even tiny quantities can be hazardous [6]. As for halides, chlorides are the most abundant in syngas after gasification, and they can also contaminate the catalysts. Nonetheless, a few studies [19,20] have concluded that chloride compounds had a negligible influence on the catalytic performance. Regarding the particulate matter, they can cause fouling, corrosion, and erosion and if it is not treated properly, it could have an impact on efficiency and safety. Tars are made up of organic compounds that can condense, and the problems they cause are similar to those associated to the particles [6].

Alkali metals consist primarily of potassium and, to a lesser extent, sodium [21]. The alkali concentrations present in biomass can contaminate catalysts due to their sensitivity to their presence [22]. Potassium is an essential alkali metal present in most biomass feedstocks [23,24,25]. Its behaviour in cobalt-based catalysts has been extensively studied [22,26], and it is well known that it reduces activity while increasing C_{5+} selectivity and reducing methane. However, it has been studied with techniques as aerosol deposition, but still research regarding contaminant in the syngas is missing.

Several studies [27,28,29] have focused on this clean-up for FTS. The Table 2.2 below provides an overview of some of the most prevalent techniques for removing contaminants from syngas:

Table 2.2. Common pathways to syngas cleaning [30]

Contaminant	**Conventional removal process**
Particle, alkali and HCl	Cyclones, filters, scrubbers, and packed bed with sorbents
Acid gas and inorganic components removal	Scrubbers and conventional chemical removal processes
H_2S and COS	Amine unit
CO_2	Adsorption, absorption, or cryogenic membranes

In addition to these procedures, syngas can be treated to tailor the H_2/CO ratio to the requirements of each application.

2.2 Fischer-Tropsch synthesis

FTS is currently gaining great importance and interest for its ability to produce liquid hydrocarbons through a clean and environmentally friendly technology. In broad terms, syngas is converted into liquid hydrocarbons in a single step via a polymerization reaction that takes place on the surface of a catalyst during FT synthesis [13].

2.2.1 Fischer-Tropsch Products

Recent concerns regarding climate change have made the use of renewable energies as an alternative to fossil fuels increasingly important. In this way, biomass could be an extremely useful resource for producing biofuels such as methanol, ethanol, dimethyl ether, synthetic natural gas, hydrogen, among others after gasification to syngas [14]. To enhance the chemical conversion and the quality of the fuels, catalytic routes have been widely studied. Figure 2.3 depicts the various potential catalytical reaction pathways by which syngas can be converted [9]. FTS is among the most significant because its products are primarily composed of hydrocarbons.

Basically, a mixture of gaseous hydrocarbons (light olefins C_1-C_4) and liquid hydrocarbons (C_{5+}) is produced after the Fischer-Tropsch process. Figure 2.4 below summarizes the products obtained and the most significant prospective applications.

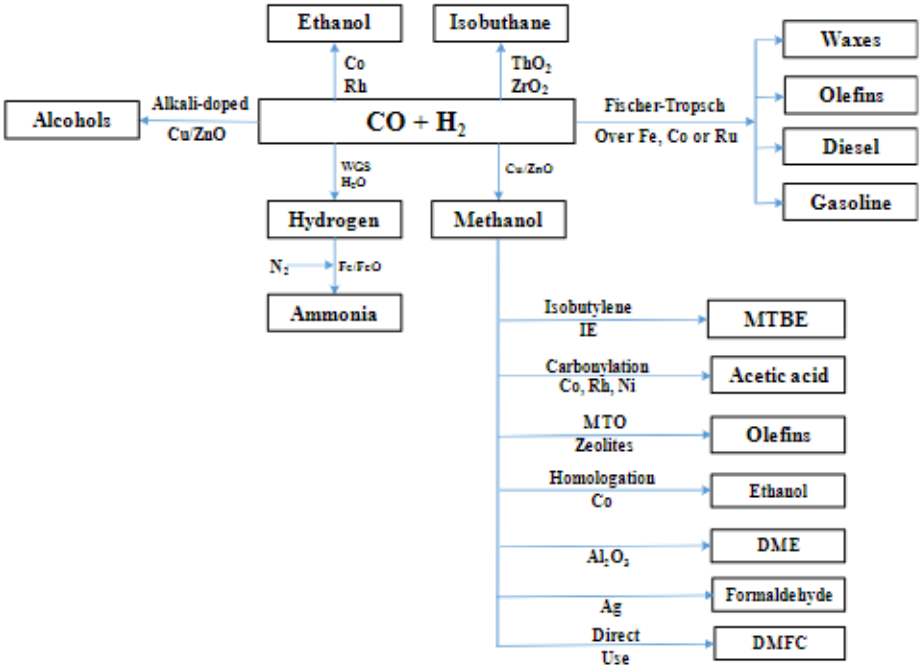

Figure 2.3. Possible syngas conversion routes [9]

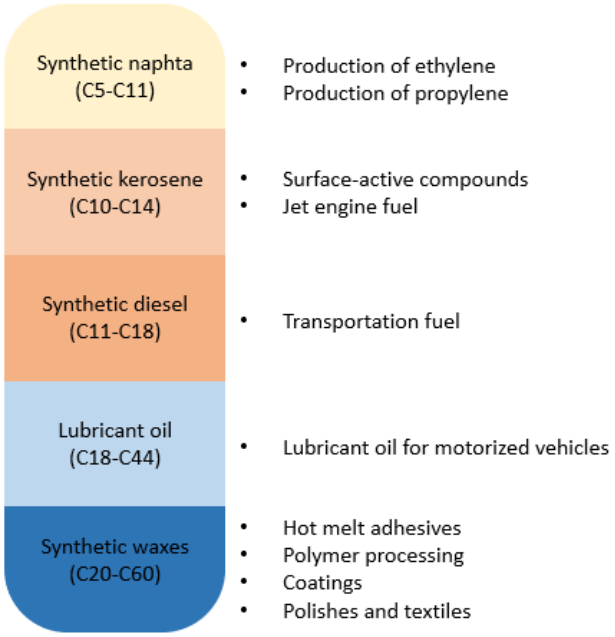

Figure 2.4. Products and potential applications after FTS [31]

Among the FTS products, light olefins are undoubtedly the most desirable, especially ethylene and propylene. They are one of the basic compounds in the petrochemical industry, considered as building blocks [32]. The annual demand for ethylene is more than 155 million tons [33] and after transportation fuels, they are the second-most-produced products in the petrochemical industry. Their value resides in

the versatility with which they can produce derivatives, such as plastics, polymers, fibres, among others [34]. The typical technique of production is Steam Cracking (SC). As it presents several environmental and economic challenges, it is necessary to develop alternative processes, such as Fischer-Tropsch.

2.2.2 Chemistry

The main reaction that takes place in the FTS is reflected in Equation 2.1 [35]. Long-chain hydrocarbons and water are obtained from the syngas produced through biomass gasification.

$$nCO + 2nH_2 \rightarrow (-CH_2-)_n + nH_2O \quad (2.1)$$

Equations 2.2 to 2.5 [13] summarize the principal reactions that occur and the products obtained during the synthesis process.

Alkanes $$nCO + (2n+1)H_2 \rightarrow C_nH_{2n+2} + nH_2O \quad (2.2)$$

Alkenes $$nCO + 2nH_2 \rightarrow (CH_2)_n + nH_2O \quad (2.3)$$

Alcohols $$nCO + 2nH_2 \rightarrow H(CH_2)_{nOH} + (n-1)H_2O \quad (2.4)$$

Carbonyls $$nCO + (2n-1)H_2 \rightarrow (CH_2)_nO + (n-1)H_2O \quad (2.5)$$

In addition to these, two main side reactions take place in the FTS, outlined by the Equations 2.6 and 2.7 [3].

Water Gas Shift Reaction $$CO + H_2O \rightarrow CO_2 + H_2 \quad (2.6)$$

Boudouard Reaction $$2CO \rightarrow C + CO_2 \quad (2.7)$$

Basically, during the Fischer-Tropsch process, the two reactants CO and H_2 adsorb on the catalyst surface, which is where the reaction takes place for the formation of the chain initiator. The reaction continues by chain propagation and ends by chain termination and product desorption. The composition of these final compounds depends significantly on the implemented catalyst and the reaction conditions. In other terms, FTS implies both a CO hydrogenation reaction and a polymerization reaction [35].

In the first, the C-O bond is broken to create new C-H compounds. In the second, the hydrocarbon chain expands through the formation of C-C bonds.

FTS implies a highly exothermic reaction [9], so temperature control is essential. The formation of one mole of monomer -CH_2- involves a release of 145 kJ [36]. In addition to the temperature, the stoichiometry of the reaction is significantly governed by the H_2/CO ratio. Depending on its value, CO conversion, the selectivity towards light olefins, the product distribution and the chain growth will be greatly affected [9]. The extent of the side reactions (Equations 2.6 and 2.7) has a significant impact on the ratio [3]. The choice of catalyst is crucial to minimize as much as possible these two side reactions and maximize the yield of light olefins. In addition, it is desirable to avoid producing methane, the most undesirable by-product of FT.

2.2.3 Kinetic Mechanism

The Fischer-Tropsch reaction consists of a step-by-step addition polymerization reaction and is based on the Langmuir-Hinshelwood-Hauguen-Watson mechanism [3]. There are numerous kinetic mechanisms that can explain the FT reaction. Figure 2.5 below depicts the alkyl mechanism, one of the most prevalent and acknowledged kinetic mechanism [3].

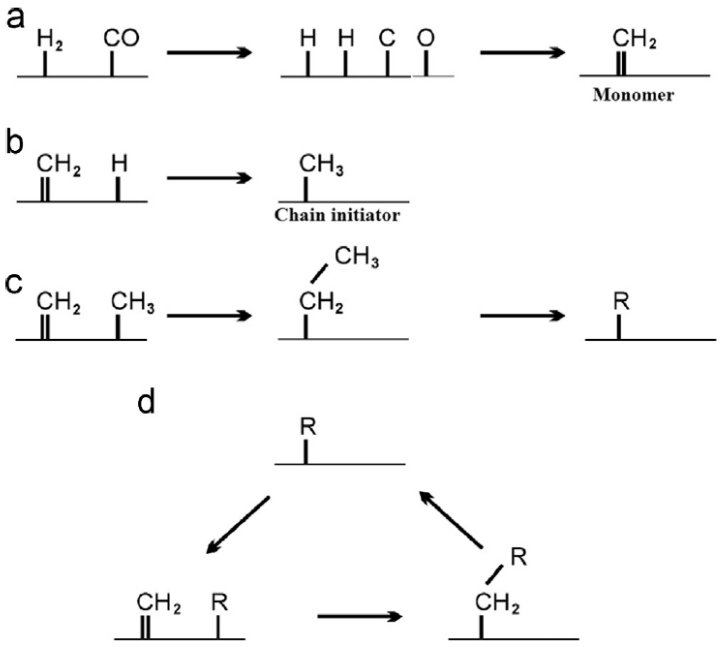

Figure 2.5. Alkyl mechanism overview: (a) Monomer formation; (b) Chain initiator obtention; (c) Chain growth and (d) Propagation [3]

As can be seen, four separate stages occur during the reaction. First, H_2 and CO initially adsorb and dissociate on the catalyst surface, producing CH_2 as a monomer (Figure 2.5-a). The remaining oxygen can either react with hydrogen to produce water or with carbon monoxide to form CO_2. When the monomer reacts with more of the hydrogen molecules adsorbed in the surface, CH_3 is formed (Figure 2.5-b). This compound acts then as a chain initiator. Its combination with more monomer molecules results in the growth of the hydrocarbon chain (Figure 2.5-c). In other words, the chain is progressively growing with successive incorporation of CH_2.

Hydrogenation and desorption reactions are known to be the possible pathways for terminating chain propagation [37]. The product can be formed either by hydrogen addition in surface leading to n-paraffins (Figure 2.6-a) or β-hydride elimination leading to α-olefins (Figure 2.6-b). The initial desorbed molecules may compete with gas-phase CO molecules for adsorption on the catalytically active centres, re-adsorb and continue reacting [37].

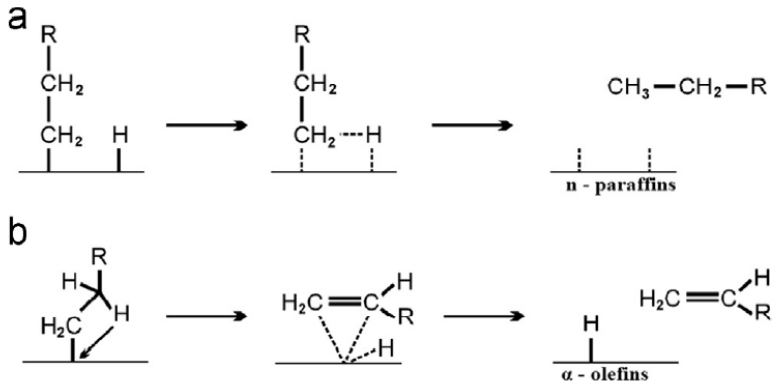

Figure 2.6. Possible alkyl chain growth termination mechanisms: (a) hydride termination and (b) β-hydride elimination [3]

2.2.4 Chain Growth Probability

Equation 2.8 [38] is known as the Anderson-Schulz-Flory (ASF) distribution. It consists of a statistical function that reflects the product carbon number distribution of the product formation. This model assumes that chain growth occurs one carbon at a time, step by step by polymerization and it is followed by the FT reaction [35].

$$\log\left(\frac{w_i}{i}\right) = i\log\alpha + \log\left(\frac{(1-\alpha)^2}{\alpha}\right) \tag{2.8}$$

In the Equation above, w_i is the weight fraction of a compound, *i* refers to the hydrocarbon chain length and α is the chain growth probability.

The model also assumes that the probability of chain growth is independent of the chain length. With this reasoning it is possible to determine the product distribution from the following Equations 2.9-2.11 [38], where N_0 represents the initial elements and C_n the products formed successively.

C1-products $$N_1 = N_0 \cdot (1 - \alpha) \quad (2.9)$$

C2-products $$N_2 = (N_0 - N_1) \cdot (1 - \alpha) = N_0 \cdot \alpha \cdot (1 - \alpha) \quad (2.10)$$

Cn-products $$N_n = N_0 \cdot \alpha^{n-1} \cdot (1 - \alpha) \quad (2.11)$$

Figure 2.7 below represents how the chain grows by the C-C formation and how products are formed according to this model:

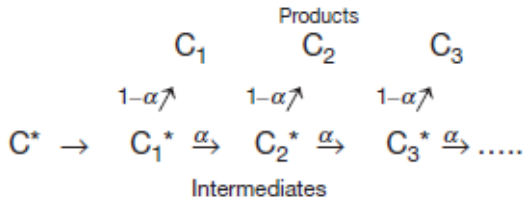

Figure 2.7. Chain growth and termination following the ASF distribution [35]

Graphically, the ASF model for product distribution in FTS as a function of chain growth probability is shown in the following Figure 2.8. The diagram displayed below depicts the product distribution predicted by Equation 2.8 for various alpha values.

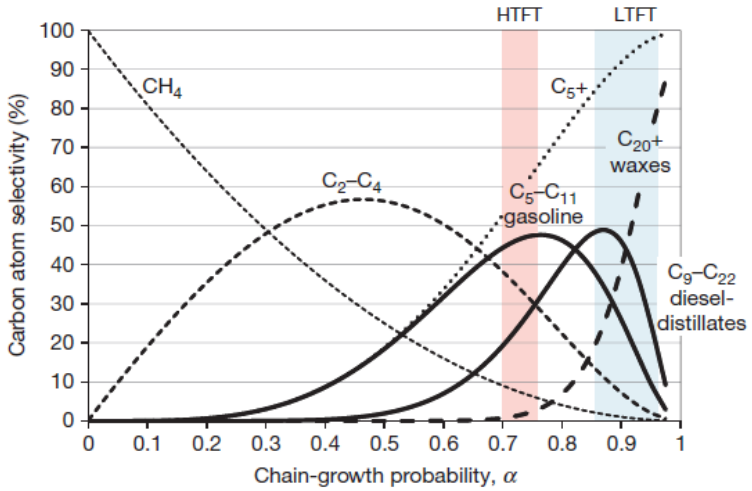

Figure 2.8. Product distribution by ASF model [38]

The α value is dependent on the catalysts employed. For instance, at low temperatures, metals such as iron and cobalt can attain alpha values of approximately 0.9, resulting in the production of primarily waxes. Whereas other metals as nickel presents low alpha values, thus producing more methane [38]. Since the primary aim of FTS is to shift the selectivity toward light olefins and avoid the production of methane, this model predicts that an α value between 0.4 and 0.5 provides the optimal selectivity [5]. In FTS the desirable value of α is around 0.7 [5]. To achieve this value, the reaction conditions can be altered: Reducing the H_2/CO ratio, decreasing the temperature and increasing the pressure can result in a high chain growth probability [38].

Experimentally, the paraffin/olefin (P/O) ratio is used to measure the selectivity towards alpha olefins, the product of value [39]. It can also be corelated with the probability of chain growth, as shown in Figure 2.9. Typically, the P/O ratio increases exponentially when the chain length exceeds a value of *n* equal to 2. From this value of chain length, the P/O ratio deviates considerably from the curve.

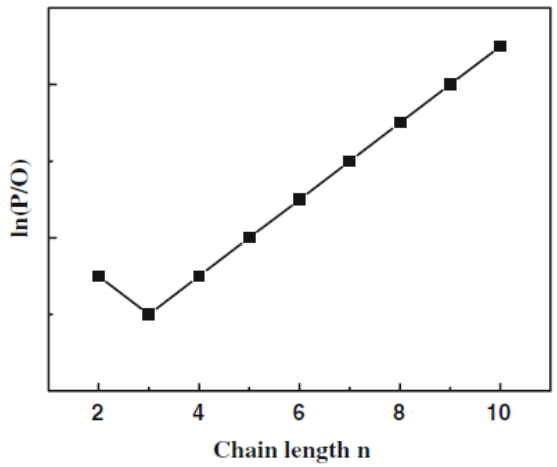

Figure 2.9. Paraffin/Olefin ratio dependence on chain length in FTS [39]

2.2.5 Fischer-Tropsch catalysts

Catalysts are the fundamental part in the Fischer-Tropsch synthesis. Not only to achieve the desired products, but also to make the process economically and environmentally viable. It is for this reason that finding a catalyst that best suits the process conditions is essential.

The catalysts used in FTS are metallic, due to their ability to form a complex bond with CO and dissociate it to the monomer [10]. The most studied and accepted catalysts

for FTS are cobalt, iron, nickel, and ruthenium because they have a sufficiently appropriate activity in this process [9]. Despite its high activity, ruthenium is discarded because its high price undermines the economic viability of the entire process. Nickel is also discarded because it exhibits a high selectivity for methane. In other terms, its chain growth is limited. Therefore, it seems that only iron and cobalt are the two metals that that suit this process better.

Iron is one of the most abundant and lowest cost materials. It is also easier to handle and presents fewer health and environmental hazards than cobalt. However, it is much more active towards the Water Gas Shift reaction than cobalt. On the other hand, cobalt-based catalysts allow working at lower temperatures than the iron-based ones, which gives more flexibility when it comes to varying the chain growth probability. Moreover, cobalt-based catalysts are able to work at higher H_2/CO ratios and with syngas produced by biomass, whereas iron-based ones are more suitable for syngas produced by coal gasification with lower H_2/CO ratios [9].

Thus, cobalt appears to be the optimal metal for Fischer-Tropsch synthesis. It presents a very reasonable balance between selectivity and activity that allows its use on a large scale. In addition, they exhibit higher productivity than iron-based catalysts would provide at lower space velocities and lower pressures [10]. Metallic cobalt is the catalytically active material [10]. Within the cobalt active sites, it is important to highlight the importance of the B5 sites, especially in the Fischer-Tropsch process [40]. It is believed that these sites require less activation energy to form a bond with CO [41,42].

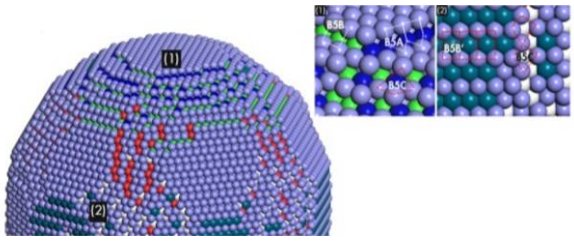

Figure 2.10. B5 sites on cobalt nanoparticle surface [40]

As shown in Figure 2.10, B5 sites are only present in the kink or terrace sites on the metal surface [42]. The number of these sites in the catalyst is highly dependent on the particle size, becoming greater when it is larger due to the increase of edges [43].

2.2.6 Support and Promoter Materials

Small-particle metals are typically unstable and tend to sinter, particularly at the temperatures required for FTS [38]. This phenomenon has a negative impact on the activity of the catalyst, so it is necessary to identify materials that hinder this deactivation process.

Supports in catalysts play a very important role in providing stability to the active phase. The catalyst activity will inevitably be affected by the nature of the support [44]. It is for that reason that the choice of a good support is a key pass in the synthesis of a catalyst. High surface area, appropriate pore size and pore volume for the type of metal, and well-defined surface chemistry are desired characteristics for these materials in order to facilitate the interaction between the metal and the support, as well as the dispersion of the metal [4]. Alumina, silica, and titania are three of the most commonly used supporters for Fischer-Tropsch type processes [3].

Alumina is the ideal support for cobalt-based catalysts [4,34]. Its high mechanical stability and excellent textural properties are some of the reasons. Furthermore, it has a high resistance to attrition and a moderate Co-support interaction strength. As a result of its relative affordability, it is the most prevalent commercially. There are three distinct phases of alumina: α, γ and η-Al_2O_3. Only the first of these is a crystalline structure, while the other two are amorphous porous structures that present spinel structures [4].

Silica is also one of the most widely used supports for Fischer-Tropsch synthesis, especially at low temperatures [34]. It is characterized by a high surface area and a narrow, well-defined pore structure. It also possesses an excellent thermal resistance. Comparatively, the interaction between cobalt and alumina is significantly weaker, which favours the reducibility of the metal. Nevertheless, the thermal stability of silica is substantially lower than that of alumina, limiting its use to high-temperature processes [38].

As for titania, it is less popular than the previous two supports but can also be a good choice for FTS [34]. It presents high thermal and chemical stability and corrosion resistance. In addition, some studies [45] have concluded that the level of interaction with cobalt is in the medium between alumina and silica. A strong interaction between

the metal and the support favours the dispersion of cobalt on the support, despite reducing the reducibility of the catalyst. However, a weak interaction between the two components implies the formation of a greater number of metal agglomerates on the surface of the support and therefore disfavours its dispersion [46].

Besides, the activity and selectivity towards the desired product can also be modified by materials known as promoters [47]. There are two different types: structural, such as alumina that provides stability to the catalyst by varying the interaction of the support with the oxide metal and therefore improving the dispersion of the metal on the support [46]; and electronic, such as K or Cs to improve the characteristics of the catalyst by modifying the surface [38]. In short, promoters are generally necessary elements to favour dispersion and selectivity towards the desired products in cobalt-based catalysts.

Noble metals, such as rhenium, are the most frequently used promoters in cobalt-based catalysts to increase the reducibility and dispersion of the active metal. However, transition metal oxides and some earth metal oxides can also be used [34]. Al, Mn, Zn, and La are some examples of these promoters. Manganese has been extensively studied [48,49,50,51] as a promoter for cobalt catalysts and can be considered both structural and electronic [49]. It has been reported that Mn is able to increase the activity of cobalt-based catalysts, the dispersion of the metal on the support and the selectivity towards C_{5+} products while decreasing it towards CH_4 [48]. However, its behaviour in the FT reaction is still largely unknown, since with different treatments, different Mn:Co ratios or different catalyst synthesis methods, the results show from positive, to negative, to no discernible effects. It is evident from the available experimental data that the promotion effect of Mn is not completely understood in FTS and therefore, it is still worthy of study.

2.2.7 Catalyst deactivation

Catalyst deactivation is one of the most important challenges in catalysis. Progressive loss of activity and/or selectivity is a problem that results in a significant economic loss due to the need for replacement [7]. Although catalysts eventually deactivate due to repeated use, in some cases this process can be avoided, postponed,

or even reversed, thus it is significantly important to understand the different mechanisms that cause the loss of activity. Deactivation is a particular problem in Fischer-Tropsch synthesis since FT catalysts are usually more sensitive than normal to possible external agents [52].

There are numerous deactivation mechanisms, but they can be briefly classified into 3 groups: chemical, mechanical, and thermal [7]. Among these, poisoning, fouling, thermal degradation, and mechanical failure are the most common ones.

Catalyst poisoning is caused by strong adsorption of reactants, products, or other impurities on the catalyst surface, leading to blockage of active sites [7]. Figure 2.11 shows an example of what is involved in catalyst poisoning: a sulphur atom is observed physically blocking an active site in the metallic surface. Furthermore, depending on the type of interaction it can electronically modify its nearest neighbour atoms.

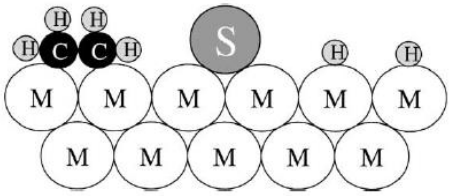

Figure 2.11. Graphical example of poisoning over a metal surface [7]

Fouling consists of the physical deposition of non-desirable substances on the catalyst surface, which again results in the physical blocking of pores, and it is closely related with carbon deposition. Figure 2.12 illustrates the possible routes for obtaining carbon deposition or "coke."

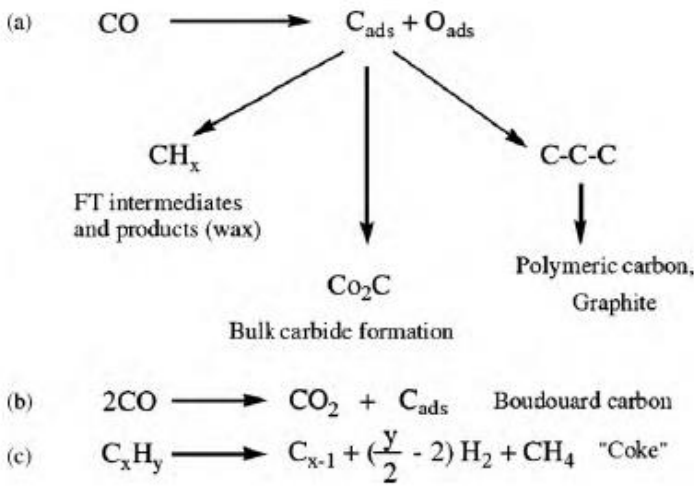

Figure 2.12. Possible carbon formation pathways during FTS in cobalt-based catalysts [53]

Carbon formation in FTS is particularly significant because it involves the production of a wide variety of hydrocarbons and carbonaceous compounds. Whether one process takes place or the other depends on several factors such as the temperature, pressure, and nature of the catalyst and feed, as well as the products that are produced.

As for thermal degradation, sintering involves the agglomeration of small particles into larger ones. In this way the activity of the catalyst is negatively affected as the surface area is reduced [54]. This phenomenon is particularly prevalent at high temperatures, which poses a significant problem for FTS, a highly exothermic process.

Lastly, crushing, attrition, and erosion are the most prevalent forms of mechanical catalyst degradation [7].

2.2.8 Effect of the biomass impurities in cobalt-based catalysts

Poisoning is especially relevant in FTS, since cobalt-based catalysts are particularly sensitive to impurities, so it is a challenge to be considered. Biomass as feedstock implies the possible presence of numerous elements that negatively affect catalyst activity.

Potassium behaviour and effect in cobalt-based catalysts has been extensively studied [11,12,22,26] in different ways but research over this topic is still uncertain. Potassium can be considered in some cases as a promoter in cobalt-based catalysts [55] but other authors [11,22] argue that its presence during the FT reaction drastically drops the catalyst activity and negatively affects the selectivity towards methane, while favouring the C_{5+} products when potassium is impregnated in the catalyst. Some others [12] confirmed that potassium involves loss of activity in the catalyst and selectivity towards methane and an increase towards C_{5+} products by aerosol deposition. However, the way in which it affects the catalyst by its presence in the syngas is still uncertain.

More potential contaminants in FTS are sulphur and chlorinated and nitrogen compounds. Particularly challenging is sulphur toxicity in cobalt-based catalysts. Sulphur has been reported in several studies [56,57] for its tendency to adsorb on metal surfaces, and they even suggest the possibility of selective adsorption in some cases.

Water is one of the primary products in FTS, and its role as a potential deactivator on cobalt-based catalysts is also widely studied [58,59,60]. Its effect over the activity is quite complex and depends on numerous variables, especially on the nature of the support. In contrast to other supports, such as titania or silica, alumina is known to have adverse effects on the activity of catalysts [59]. The formation of non-active cobalt oxides or irreducible cobalt compounds is a potential cause of these negative effects. [61]. It has been reported that water, as potassium, increases the selectivity of C_{5+} products and decreases their tendency to produce methane, regardless of differences in activity depending on the support [58] and the effect is even greater at higher partial pressures of water.

2.2.9 Fischer-Tropsch Process Conditions

The conditions under which FTS is conducted will have a significant impact on the desired product. Light olefins selectivity can be improved by operating at high temperatures and low pressures [16,62]. However, this also favours the formation of methane, which is an undesired by-product of the reaction.

Moreover, the H_2/CO ratio plays an important role in shifting the selectivity towards light olefins. If this ratio is decreased, that means that the metal surface will be more covered with CO than with H_2, thereby preventing side reactions and enhancing the conversion to olefins [16].

2.3 Catalysts synthesis

There are numerous techniques for synthesizing catalysts, including impregnation, deposition-precipitation, and electrostatic adsorption. When synthesizing FT catalysts, Incipient Wetness Impregnation (IWI) is one of the most used methods [38].

Essentially, the method involves filling the pores of the porous support with the metal species (active phase) in solution form. To add this quantity of precursor solution, it is necessary to know the precise pore volume. After impregnation, the material is dried to remove the remaining solution, and then calcined at high temperatures to degrade the present salts and produce the metallic oxide [38].

2.4 Catalyst characterization

In catalytic processes, the characterization of catalysts is of essential importance. It is necessary to understand the properties that cause catalysts to behave in particular ways.

2.4.1 N_2 Physisorption

From the N_2 adsorption-desorption technique it is possible to measure the catalyst surface area and pore volume, as well as the pore size distribution. It relies on the physical adsorption of an inert gas, the nitrogen, onto the catalyst surface [63].

The Brunauer, Emmet and Teller (BET) method is the most commonly used for this technique. It considers that the adsorption of the gas on the catalyst surface can be explained by an extension of the Langmuir model. In this model it is assumed that the number of molecules needed to form a monolayer on the surface can be determined by knowing the volume occupied by each molecule, and therefore, it is possible to determine the surface area of the catalyst. The method involves the assumption that a monolayer is formed first, followed by an infinite number of multilayers. Molecules adsorb on equivalent active sites in the first layer, and the multilayer expands to an infinite thickness until the system reaches saturation pressure. Their bonding is weak and reversible; there is no strong interaction between the molecules.

In practice, samples come into contact with liquid nitrogen at a temperature of 77 K. The volume of gas adsorbed on the surface can be related to the partial pressure of the system during adsorption, as reflected in Equation 2.12 [38]:

$$\frac{P}{V \cdot (P_0 - P)} = \frac{1}{V_m \cdot C} + \frac{(C-1) \cdot P}{V_m \cdot C \cdot P_0} \tag{2.12}$$

Where V is the adsorbed volume, V_m the monolayer volume, P and P_0 the nitrogen partial and saturation pressure, respectively, and C is the BET constant. If $P/V \cdot (P_0-P)$ is plotted versus P/P_0, it is obtained a line whose slope and intersection are given by Equations 2.13 and 2.14 [38]. From these, it is possible to estimate the adsorbed volume in the monolayer.

$$slope = \frac{C - 1}{V_m \cdot C} \tag{2.13}$$

$$intersection = \frac{1}{V_m \cdot C} \tag{2.14}$$

Once V_m is known, Equation 2.15 [38] can be used to calculate the BET Surface Area (S_{BET}). In the Equation below, N_A is the Avogadro number, A_x refers to the cross-sectional area of the particle and $_v$ to the molar volume.

$$S_{BET} = \frac{V_m \cdot N_A \cdot A_x}{v} \tag{2.15}$$

In contrast, the Barret, Joyner, and Halenda (BJH) method allows the determination of pore size and its distribution. In practice, the procedure is identical to the BET methodology. This procedure can be described by the Kelvin model of pore filling, described in the Equation 2.16 [38], where P/P_0 is the relative pressure at equilibrium, γ the surface tension of the liquid condensate, V_m the molar volume of the liquid condensate, r_K the Kelvin radius (the radius of the pore), R the universal ideal gas constant, and T refers to temperature.

$$ln\frac{P}{P_0} = \frac{2 \cdot \gamma \cdot V_m}{r_K \cdot R \cdot T} \tag{2.16}$$

In this case, the quantity of gas adsorbed on the surface in the descending region of the BET adsorption isotherm is determined.

2.4.2 H_2 Chemisorption

Chemisorption is one of the most popular techniques for characterizing metal-based catalysts in order to obtain their dispersion and particle size. It is founded on the measurement of the amount of adsorbed gas, in this case hydrogen, on the surface of the metal as a function of system pressure. This method assumes that hydrogen molecules form strong bonds with the active sites of the metal selectively [64].

The Langmuir model is one of the most appropriate when analysing this adsorption isotherms. This model follows the Equation 2.17 [38], which is used to calculate the metal dispersion, D_{chem} (%), under isothermal conditions.

$$D_{chem} = \frac{V_m \cdot N_A \cdot F_S}{V_{mol} \cdot N_T} \cdot 100 \quad (2.17)$$

As for the rest of the terms in the equation, V_m refers to the monolayer adsorption volume (cm^3/g), N_A to the Avogadro constant, F_S the stoichiometry factor, V_{mol} is the volume occupied by one molecule of gas (22414 cm^3 STP/mol of gas), and N_T the total number of metal atoms.

Furthermore, once the dispersion value is known, it is possible to determine the particle size (d_p). Using the site density of cobalt (14.6 atoms/nm^2) and assuming spherical particles, Equation 2.18 [65]. can be used to determine its value.

$$d_p = \frac{96}{D_{chem}} \quad (2.18)$$

2.4.3 X-Ray Diffraction

X-ray diffraction (XRD) is an effective method for determining the structure and composition of crystalline samples. It is a fast analytical technique that allows the identification of crystalline phases and can also provide information on particle size [63]. It features numerous advantages, as it permits rapid analysis of the crystalline structure of the sample. However, neither the degree of crystallinity nor the presence of amorphous phases can be determined [63].

The analysed material is finely crushed and placed homogeneously and as flat as possible on a specific holder. Using the proper equipment, the sample is subjected to an X-ray beam of a particular wavelength. The specific lattice planes then generate peaks that can be associated with particular compounds based on their angular positions (2Θ). The technique relies on the Braff relation represented in Equation 2.19 [63] for the calculation of lattice distances. The reflection corresponds with *nr*, λ is the wavelength of the X-rays, d the distance between two lattice planes and Θ is the angle formed by the rays traveling in the direction of the sample surface and the normal direction.

$$n_r \cdot \lambda = 2 \cdot d \cdot sin\theta \quad (2.19)$$

The crystal size can be calculated using Scherrer's formula, which is reflected in the following Equation 2.20 [38]. It is defined by *L*, which measures the length of the particle in the direction perpendicular to the plane axis. The X-ray wavelength is

represented by λ, β is the peak width, and Θ the angle between the rays directed toward the sample surface and the normal plane.

$$L = \frac{K \cdot \lambda}{\beta \cdot cos\theta} \tag{2.20}$$

From this method it is also possible to calculate Co_3O_4 crystal size and dispersion. Equation 2.21 [66] represents the metallic crystal size, d_c, calculated from τ, the crystallite size measured during XRD analysis and a factor (0.75) that involves the relative molar volumes of metallic cobalt and Co_3O_4. Knowing d_c and assuming again spherical particles of cobalt, the dispersion can be determined from Equation 2.22 [65].

$$d_c = 0.75 \cdot \tau \tag{2.21}$$

$$D_{XRD} = \frac{96}{d_c} \tag{2.22}$$

2.4.4 Temperature Programmed Reduction

In order for the catalyst to be active and capable of producing the surface reaction, it must be reduced. The Temperature Programmed Reduction (TPR) technique enables qualitative and quantitative analysis of different characteristics of the catalyst, such as its most relevant reduction temperatures, the ease or difficulty of reduction or the capacity of H_2 consumption [67].

In practice TPR consists of treating a precursor oxide with a stream of reactive gas (usually H_2) while progressively increasing the temperature. Equation 2.23 [4] represents the relationship between the Gibbs free energy ΔG (kJ/mol) with the ratio of water to hydrogen pressures (P_{H2O} and P_{H2}). Also, $\Delta G°$ represents the standard Gibbs free energy (kJ/mol), R the ideal gas constant and T the temperature. This reduction is only feasible if thermodynamics allows it, that is, for oxides whose standard free energy of reduction is negative.

$$\Delta G = \Delta G° + RT \cdot \log\left(\frac{P_{H_2O}}{P_{H_2}}\right) \tag{2.23}$$

In cobalt-based catalysts, two peaks are expected from the TPR profile, corresponding to the reduction reactions in Equations 2.24 and 2.25 [17]:

$$Co_3O_4 + H_2 \rightarrow 3CoO + H_2O \quad (2.24)$$

$$CoO + H_2 \rightarrow Co + H_2O \quad (2.25)$$

2.4.5 X-Ray Fluorescence

X-Ray Fluorescence (XRF) is an analytical method used to determine the elemental composition of a material in any physical state. It is a fast and non-destructive, technique that requires only a small amount of sample. The material is subjected to a beam of X-rays. Consequently, the elements present in the sample emit a fluorescent radiation with an energy that is characteristic of each species, allowing its identification [68].

2.4.6 Scanning Transmission Electron Microscopy

Scanning Transmission Electron Microscopy (STEM) is a widely used technique for the measurement of the electronic structure and composition of the deeper structures of a material [69]. In practice an electron beam is passed through the analysed sample. The scattered electrons and the atoms ionized by the energy beam emit a signal that is recorded and can be associated to the different components that form the material.

Different procedures have been developed within this method. Energy Dispersive X-Ray (EDX) analysis facilitates the obtention diffraction patterns to identify crystalline phases. The emitted rays are characteristic of each element and therefore allow the identification of the composition of a specific part of the sample. An important limitation of this method is that there must be sufficient contrast between the particles and the support for the analysis to be effective [38].

2.5 Catalyst testing

The use of a fixed bed reactor for catalyst testing has the advantage that it provides greater flexibility when testing at different scales and does not require a separation stage to recover the catalyst after the reaction [9]. Also, it is possible to use smaller catalyst particles, since intraparticle diffusion is not a problem [4]. That is why the fixed bed is one of the most widely used reactors at different scales to study the

main characteristics of catalysts. When testing a catalyst, the aim is to determine three basic characteristics: activity, selectivity, and stability.

2.5.1 Activity

There is a clear need to search for catalysts with high activity, translated into high productivity with relatively small volumes [64]. In FTS, activity is typically measured in terms of conversion and Turnover Frequency (TOF), represented through the Equations 2.26 and 2.27 [38].

$$x_{CO} = \frac{F_{CO_0} - F_{CO}}{F_{CO_0}} \tag{2.26}$$

$$TOF = \frac{r \cdot M_m}{x_m \cdot D} \tag{2.27}$$

In terms of molar flow rate (mol/h), the conversion reflects the quantity of CO converted (F_{CO0}-F_{CO}) relative to its initial concentration in the inlet stream (F_{CO0}). Moreover, the TOF is explained as the number of molecules reacting at each available catalytic site per unit time. In the above equation, r refers to the reaction rate (mol/g_{cat}·s), defined through the Equation 2.28 [38], M_m the molecular weight of the active metal, in this case cobalt (g/mol), x_m the weight fraction of the metal and D its dispersion (%).

$$r = \frac{F_{CO_0} \cdot x_{CO}}{m_{cat}} \tag{2.28}$$

Site Time Yield (STY) is also a common way of measuring activity. It has the same meaning as TOF but assumes that every atom on the surface of the metal is an active site.

2.5.2 Selectivity

The selectivity of a catalyst can be defined as the ability to produce the desired product within a distribution [38]. It depends significantly on several conditions such as the temperature and pressure of the system, the space velocity of the compounds involved, the composition in the feed, the geometry and type of reactor and, mainly, the degree of conversion. This is why it is so important to keep the conversion constant when comparing the selectivity on different catalysts.

Selectivity towards a desirable product B can be determined by Equation 2.29 [38], where F_i refers to molar flow rates and x_{CO} to CO conversion.

$$S_B = \frac{F_B}{F_{CO_0} \cdot x_{CO}} \tag{2.29}$$

2.5.3 Stability

The degree of a catalyst stability refers to the length of time it maintains a reasonable level of activity and selectivity. It is essential to find highly stable catalysts, particularly at commercial levels. This property depends on a variety of factors, but especially on the deactivation of the catalyst [70]. During use, a reasonably stable catalyst will degrade very slowly. However, after repetitive use, it will inevitably deactivate at some point.

2.6 Soxhlet Extraction

Soxhlet extraction appears to be a viable technique for removing the hydrocarbons generated by the Fischer-Tropsch reaction catalyst [60].

This form of extraction involves using the condensed vapours of a particular solvent to extract the undesirable catalyst components. These vapours come into contact with the sample, and the soluble portion of the sample is then combined with the solvent [71]. The following Figure 2.13 depicts the installation configuration.

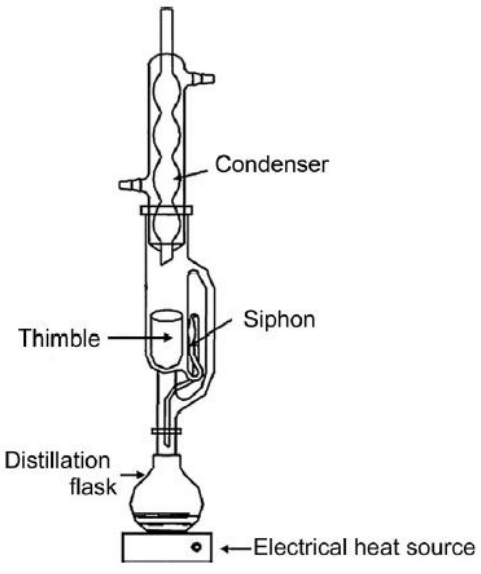

Figure 2.13. Soxhlet extractor configuration [71]

In practice, the catalyst is placed in a cellulose thimble within the main chamber of the setup. This chamber is connected to a round-bottom flask filled with solvent and a condenser that cools the gases to prevent them from escaping into the atmosphere. The electrical heat source boils the solvent, which then rises to the main chamber and condenses once more. When the liquid reaches the excess level, the siphon draws it back into the flask in order to repeat the same process. The latter is part of an extraction cycle and can be repeated as many times as necessary to obtain the optimum extraction yield.

3 Experimental methods

Earlier work partially influenced this chapter, since most of the experimental methodologies are identical [1].

3.1 Catalyst synthesis

Four different types of catalysts were prepared during the study. The IWI method was used to accomplish the synthesis of all of them. First, the support is impregnated with manganese as a promoter in the form of $Mn(NO_3)_2$-$4H_2O$ dissolved in deionized water. Three different supports were used: γ-Alumina Sasol Puralox SCCa 45/190, Silica Davisil Grade 62 from Sigma-Aldrich and Titania Degussa P25. In order to avoid diffusion limitations, the supports were sieved to obtain a particle size between 54 and 90 µm prior to impregnation. After this first impregnation, they are dried overnight in a convection oven at 110 °C, attempting to prevent the formation of agglomerates and ensure uniform drying throughout the catalysts by stirring the sample at regular intervals. The mixture of support and promoter is then calcined in a quartz tube reactor in an in-house built set up at 300 °C for 10 hours with a heating rate of 1°C/min under an air-flowing atmosphere.

Then, the impregnation of cobalt as the active material in the form of $Co(NO_3)_2 \cdot 6H_2O$ dissolved in deionized water is carried out. Also, a small volume of $HReO_4$ is added to enhance the catalysts dispersion and reducibility [59,72]. After cobalt impregnation, the catalysts are dried overnight and calcined under the same conditions as the initial cobalt impregnation. The final composition of these three catalysts is 15 wt% cobalt, 3.75 wt% manganese and 0.5 wt% rhenium.

The fourth catalyst consist of a cobalt-based catalyst with γ-Alumina Sasol Puralox SCCa 45/190 as supporter and manganese as promoter with a composition of 10 wt% cobalt, 3.75 wt% manganese and 0.5 wt% rhenium. Appendix A contains the calculations conducted to obtain the desired amounts of each compound.

The Figure 3.1 depicts an overview of the catalyst synthesis procedure, followed by a summary of the prepared catalysts in the Table 3.1.

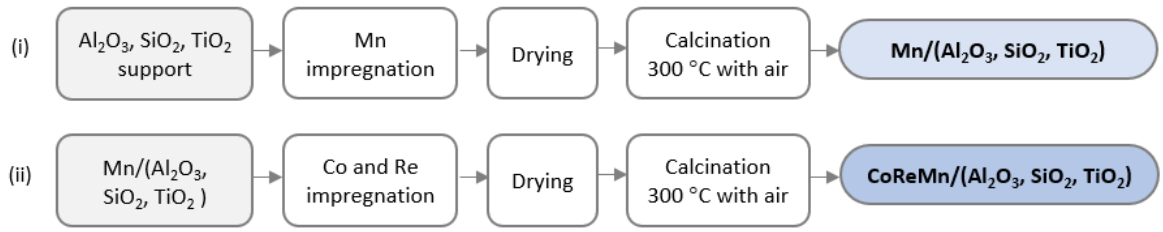

Figure 3.1. Incipient Wetness Impregnation method for the synthesis of the catalyst: (i) Manganese impregnation on the support (ii) Cobalt impregnation

Table 3.1. Overview of all the prepared catalysts

Name	Composition	Conditions
CoReMn/Al_2O_3	15 wt% Co, 3.75 wt% Mn, 0.5 wt% Re	Calcined at 300 °C during 10 hours under air as flowing atmosphere
10CoReMn/Al_2O_3	10 wt% Co, 3.75 wt% Mn, 0.5 wt% Re	
CoReMn/SiO_2	15 wt% Co, 3.75 wt% Mn, 0.5 wt% Re	
CoReMn/TiO_2	15 wt% Co, 3.75 wt% Mn, 0.5 wt% Re	

3.2 Potassium Solutions Preparation

For the study of catalyst deactivation, different potassium solutions of KNO_3, K_2SO_4, KCl and KOH were prepared at concentrations of 70 and 700 ppm in 100 mL of deionized water. The required amounts for each solution were calculated in advance and the results are given in Appendix A.

3.3 Fischer-Tropsch synthesis

The reaction is carried out at 240 °C and 5 bar with a 1.7 ratio of H_2/CO in a fixed bed stainless steel tubular reactor (10 mm i.d.), where 1 g of catalysts diluted in 19 g of SiC is placed. Silicon carbide is combined with the catalyst to reduce limitations caused by mass transfer, hot spots, and the exothermicity of the reaction. The mixture is fixed between two plugs of quartz wool trying to achieve the same bed length in every loading.

The testing of the catalyst is carried out in an in-house built laboratory-scale setup, whose flowsheet is depicted in the following Figure 3.2. The reactor is placed

inside an electric furnace fitted with a thermocouple to regulate the temperature and covered with an aluminium block in order to enhance a uniform heat transfer. The wax and liquid products are separated and collected in a hot and cold pot while the gases are analysed in a Gas Chromatograph (GC).

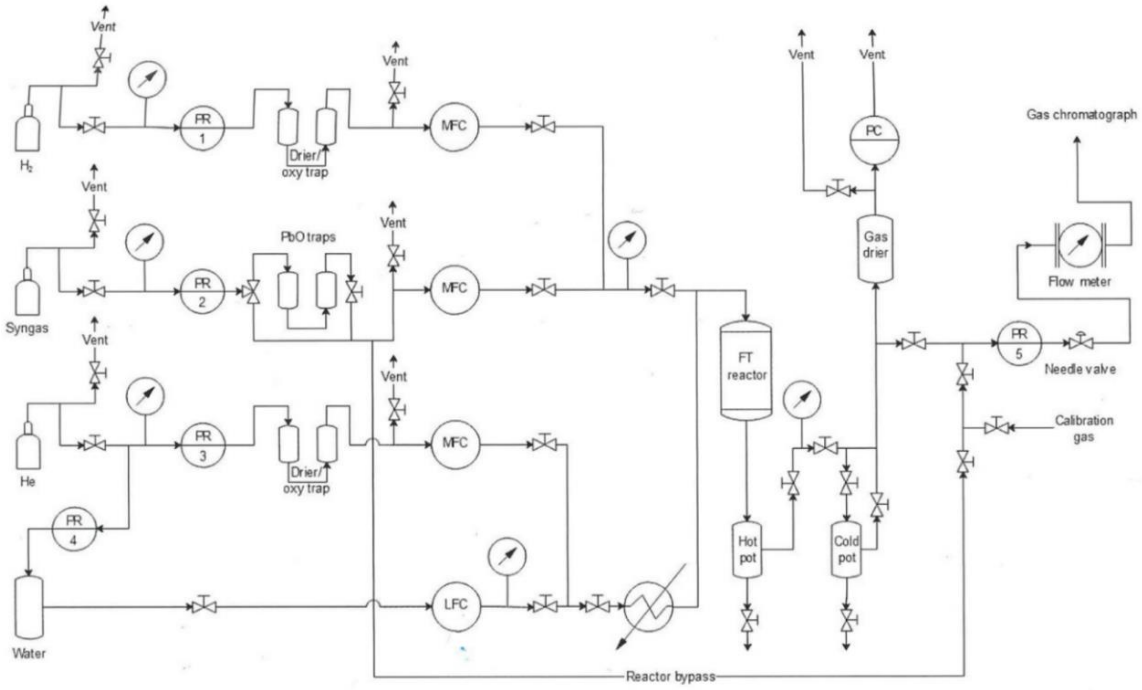

Figure 3.2. Fischer-Tropsch installation flowsheet

Throughout the performance, three distinct procedures occur: first, a leak test is carried out with 250 mL/min of He at 20 bar. Next, the catalyst needs to be reduced. The reduction is carried out in situ with a flow rate of 125 mL/min of H_2 and 125 mL/min of He. The temperature gradient increases from room temperature to 200 °C at a rate of 2°C/min. Upon attaining this temperature, the rate slows to 1 °C/min, and the temperature continues to rise until it reaches 350 °C, where it is maintained for 10 hours. After this time, the reactor temperature is reduced to 160 °C and 5 bar of He pressure is applied.

After this, the reaction can be initiated. Regarding the temperature gradient, it begins at 170 °C and rises to 225 °C at a rate of 20 °C/min. Once 225 °C is achieved, the rate is reduced to 5 °C/min until the desired reaction temperature of 240 °C is reached. At this stage, the reaction can go on for 30 hours, while the exhaust gas is analysed by the GC every hour.

The GC used for the experiments is an Agilent Technologies 6890N containing a packed Carbosieve S-II column with a Temperature Conductivity Detector (TCD) and a GS-Al_2O_3 PLOT column with a Flame Ionization Detector (FID). As for the TCD detector, the H_2, CO, CO_2 and CH_4 are calibrated and there is a 3% of N_2. Since the area of nitrogen is constant, the CO area in the feed is known and its area in the outlet is analysed every hour, it is possible to calculate the conversion of CO by the Equation 2.30, where A_{CO0} is the chromatography area of CO in the feed, A_{CO} its area in the outlet and A_{N2} the N_2 chromatography area.

$$x_{CO} = 1 - \frac{A_{CO}/A_{N_2}}{A_{CO_0}/A_{N_2}} \tag{2.30}$$

Regarding the flame ionization detector, it is where the concentration of hydrocarbons is measured. The signal is calibrated for C_1, C_2, C_3 and C_4 with the effective and response numbers. Hence, knowing the exact amount of each component it is possible to close the mass balance and know the concentration of the C_{5+} species, which is the remainder. The selectivity of the species is also calculated through the relation of the calibrated species and its relative response numbers.

3.3.1 Catalyst Poisoning

For the study of catalyst deactivation, different potassium salts were added on the catalyst bed during the course of the reaction by a syringe pump. The following Figure 3.3 shows the installation of the syringe within the setup. The solutions will evaporate in the reactor inlet and yield K compound directly into the catalysts bed.

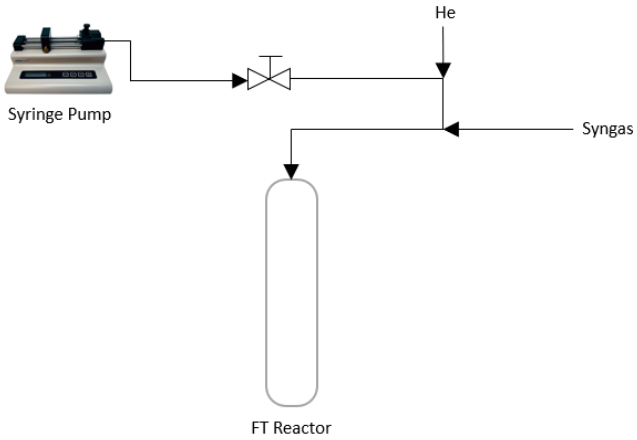

Figure 3.3. Syringe pump configuration in the reactor inlet

Several concentrations of KNO_3, KOH, K_2SO_4 and KCl were tested on the different catalysts. All solutions were added with the same volume of 8 mL. After 8 hours of regular reaction the first solution is added at 2 mL/min and a second higher concentration solution is added after 24 hours at same rate. In general, the first addition consists of a 70 ppm solution and the second of 700 ppm, but other variations were also tested. The following Table 3.2 lists the different experiments performed, the different potassium solutions added and the experimental conditions. Also, tests with water were performed as a reference. In some of the experiments, the addition rate of the solutions was also altered, but the volume of them was always 8 mL. Experiment 13 was repeated by modifying the distribution of the catalyst bed.

Table 3.2. Summary of the experiments performed

Exp no.	Catalyst	1st addition	2nd addition	Rate (mL/h)
1	$CoReMn/Al_2O_3$	KNO_3 500 ppm	KNO_3 5000 ppm	1
2	$CoReMn/Al_2O_3$	KOH 500 ppm	KOH 5000 ppm	1
3	$CoReMn/Al_2O_3$	KCl 500 ppm	KCl 5000 ppm	1
4	$CoReMn/Al_2O_3$	K_2SO_4 500 ppm	K_2SO_4 5000 ppm	1
5	$CoReMn/Al_2O_3$	KNO_3 70 ppm	KNO_3 700 ppm	2
6	$CoReMn/Al_2O_3$	KCl 70 ppm	KCl 700 ppm	2
7	$CoReMn/Al_2O_3$	K_2SO_4 70 ppm	K_2SO_4 700 ppm	2
8	$CoReMn/Al_2O_3$	H_2O	H_2O	2
9	$CoReMn/Al_2O_3$	KCl 700 ppm	-	2
10	$CoReMn/SiO_2$	KNO_3 70 ppm	KNO_3 700 ppm	2
11	$CoReMn/TiO_2$	KNO_3 70 ppm	KNO_3 700 ppm	2
12	$10CoReMn/Al_2O_3$	KNO_3 70 ppm	KNO_3 700 ppm	2
13	$10CoReMn/Al_2O_3$*	KNO_3 70 ppm	KNO_3 700 ppm	2

3.4 Catalyst dewaxing

Upon completion of the reaction, the catalyst was removed from the reactor. Due to its metallic nature after reduction, cobalt combined with silicon carbide was separated using a magnet.

The dewax was done through by Soxhlet extraction. A cellulose thimble containing approximately 0.7-0.8 grams of spent cobalt was inserted into a siphon, the primary chamber of the extractor. It was then placed in a round bottom flask containing 200 mL of n-pentane, which was heated to approximately 35-40 °C to boil. After 24 hours of extraction, the dewaxed catalyst is removed from the thimble and dried overnight in a convection oven at 90 °C.

3.5 Catalyst characterization

Characterization of the catalyst is performed both before the reaction (fresh catalyst) and after the FTS (spent) in order to observe the physical and chemical changes after the reaction and to verify that the potassium was reaching the catalyst bed.

3.5.1 N_2 Physisorption

Nitrogen adsorption-desorption was performed using the Micromeritics Tristar II 3000 Surface Area and Porosity Analyzer. Surface areas, pore sizes and pore volumes of the catalysts are calculated using the BET and BJH methodologies.

A weighted quartz tube was filled with approximately 200 mg of catalyst. Prior to analysis, sample pre-treatment is required. For this purpose, the tubes were placed in a VacPrep 061 Degasser Unit at room temperature for one hour and overnight at 200°C. Once the pressure has decreased to approximately 100 mTorr, they are cooled back to room temperature and the exact weight of the samples is noted, as the results are reflected per gram of catalyst. After this process, the reactors are placed in the equipment, where they are analysed with liquid nitrogen at 77 K.

3.5.2 H_2 Chemisorption

The dispersion and the particle size of the metal in the catalyst was measured by chemisorption with hydrogen. The Micrometrics ASAP 2020 instrument is available for this purpose.

Around 150 mg of sample was introduced in a quartz reactor placed between two portions of quartz wool. Due to the fact that the analysis is performed per gram of catalyst, the precise weight of the catalyst to be measured was recorded prior to

measurement. The reactor was then connected to the equipment, which was connected to an external thermocouple at the height of the reactor bed to control the temperature. Before analysis, the first step is to perform a leak test. The sample was degassed overnight under vacuum for this purpose. When the system pressure falls below 0.003 mmHg, analysis can begin. The catalyst is first reduced for 10 hours at 350 °C at a rate of 1 °C/min. Then it is cooled down to 40 °C, temperature at which H_2 chemisorption is carried out, with a pressure from 50 mmHg to 550 mmHg. The following Table 3.3 summarizes the conditions used in each step of the analysis:

Table 3.3. Analysis conditions in H_2 Chemisorption

Task	T (°C)	Rate (°C/min)	Time (min)
Evacuation	40	10.0	60
Leak Test	40	10.0	-
H_2 Flow	350	2.0	600
Evacuation	330	10.0	60
Evacuation	100	10.0	30
Leak test	100	10.0	-
Analysis	40	10.0	-

3.5.3 X-Ray Diffraction

X-Ray Diffraction (XRD) was performed using DaVinci1-X-Ray Diffractometer to observe the crystalline structure of the catalysts.

A small amount of material is deposited in a sample holder with the entire surface being as flat and smooth as possible. The holder is then placed in the equipment and analysed during 30 minutes with a variable divergence slit (V6) and 5-75 degrees as the angular range. The obtained results are compared by using the EVA software, which includes a database that identifies the various crystalline phases present in the samples. The software can also calculate the particle size based on the highest peak of the relevant crystal (CO_3O_4) in the XRD patterns.

3.5.4 Temperature Programmed Reduction

TPR analysis was performed using the Altamira Instruments BenchCAT TPX Analyzer Hybrid instrument.

Approximately 100 g of sample were placed in a U-shape quartz reactor fixed between two portions of quartz wool. Since the analysis is performed per gram of catalyst, the exact weigh of sample was noted. The reactor is then connected to the equipment. First, a leak test takes place and then the analysis starts. The sample is degassed with Ar at 200 °C, cool to room temperature, heating in 7% H_2 in Ar (50 mL/min) with a heating ramp of 10 °C/min until 750 °C.

3.5.5 Scanning Transmission Electron Microscopy - EDX

The S(T)EM experiments were performed using a Hitachi High-Tech instrument model SU9000 equipped with an Oxford Ultim Extreme EDX-system for energy dispersive spectroscopy. The samples were crushed and fixed in a “holey carbon” supported copper mesh grids before analysing in the S(T)EM equipment.

The experiments were performed by Oscar Ivanez, Department of Chemical Engineering, NTNU.

4 Results and Discussion

This study has been carried out over the four catalysts listed in the Table 3.1. They have been tested to know how their activity and selectivity varies when poisoned with potassium and the results are also supported by their characterization after the FT reaction. The standard experiment involves the addition of 70 ppm potassium salt after 8 hours of reaction and 700 ppm after 24 hours. However, other variations as shown in Table 3.2 were also tested.

4.1 Fresh Catalyst Characterization

Prior to the reaction, the physical and chemical properties of each catalyst were determined by different characterization techniques.

The following Table 4.1 shows the surface area, pore volume and pore size of CoReMn/Al_2O_3, 10CoReMn/Al_2O_3, CoReMn/SiO_2, CoReMn/TiO_2 and the three supports (Al_2O_3, SiO_2 and TiO_2). The results were obtained after the N_2 adsorption-desorption performance, based in the BET for surface area and BJH method for pore analysis.

Table 4.1. Surface area, pore volume and pore size of fresh catalysts obtained by BET/BJH method

Catalyst	**Surface area (m^2/g)**	**Pore volume (cm^3/g)**	**Pore size (nm)**
Al_2O_3	185	0.74	13.4
CoReMn/Al_2O_3	152	0.53	11.6
10CoReMn/Al_2O_3	163	0.45	12.6
SiO_2	300	1.10	11.6
CoReMn/SiO_2	236	0.82	11.8
TiO_2	57	0.15	10.2
CoReMn/TiO_2	51	0.26	18.2

The materials should ideally have high porosity and a large surface area. CoReMn/SiO_2 has the highest surface area with 236 m^2/g and CoReMn/TiO_2 the lowest with 51 m^2/g. As expected, the addition of promoter and cobalt reduces the surface

area, pore volume, and pore size of the support, since they are impregnated into its pores. Therefore, it can be assumed that cobalt and manganese are being deposited effectively in the pores of the three different supports. On the other hand, it can also be observed that the surface area and pore size of the 10CoReMn/Al_2O_3 catalyst is slightly larger than that of CoReMn/Al_2O_3. It also fits, because in the first case fewer cobalt particles are being impregnated into the alumina.

Figure 4.1 below shows the pore size distribution of the fresh catalysts and the three supports obtained by the BJH method. Comparing with its supports, no significant changes in the distribution are observed, suggesting once again that the cobalt particles and promoters are uniformly dispersed in the pores. On the contrary, the increase in pore volume in titania when the promoter and precursor are impregnated may be due to the change in the phase produced after calcination of the catalyst during its synthesis.

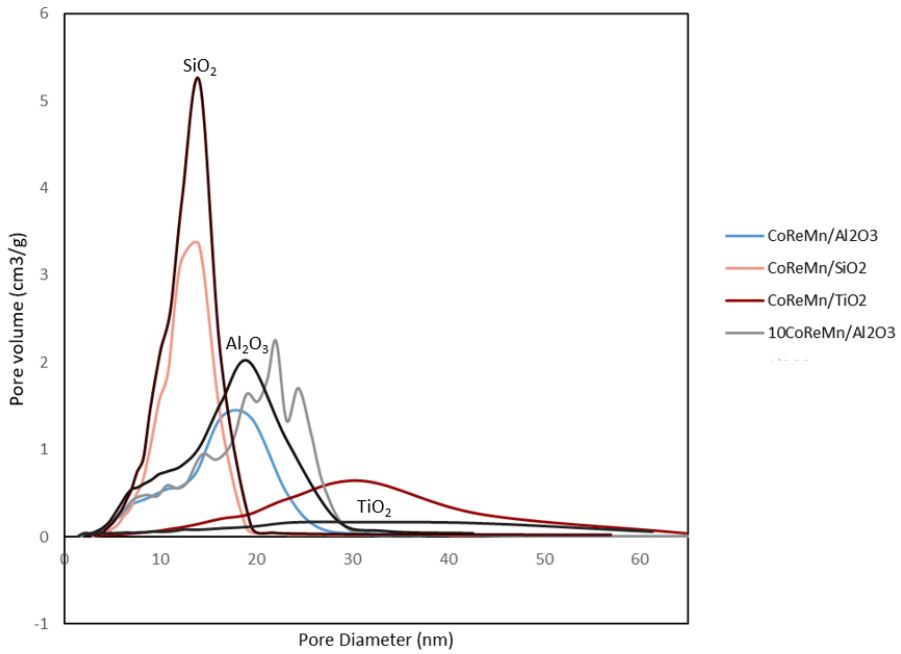

Figure 4.1. Pore size distribution of supports and fresh CoReMn/Al_2O_3, 10CoReMn/Al_2O_3 CoReMn/SiO_2, and CoReMn/TiO_2 catalysts

In order to compare the elemental composition, X-Ray diffraction was carried out and the diffractograms of CoReMn/Al_2O_3, 10CoReMn/Al_2O_3, CoReMn/SiO_2, CoReMn/TiO_2 and the three supports (Al_2O_3, SiO_2 and TiO_2) are shown in Figure 4.2. In all cases the support, cobalt and promoter phases can be identified and the support structure is maintained. The MnO_2 signal appears around 58° and cobalt in the form of Co_3O_4 around 18, 32, 45 and 65°. However, these cobalt-signals disappear when the

loading of the metal precursor in the catalyst is 10%, suggesting that perhaps in this case the cobalt phase is sufficiently amorphous that its identification is not possible. The fact that the particle size is smaller may also be a contributing factor.

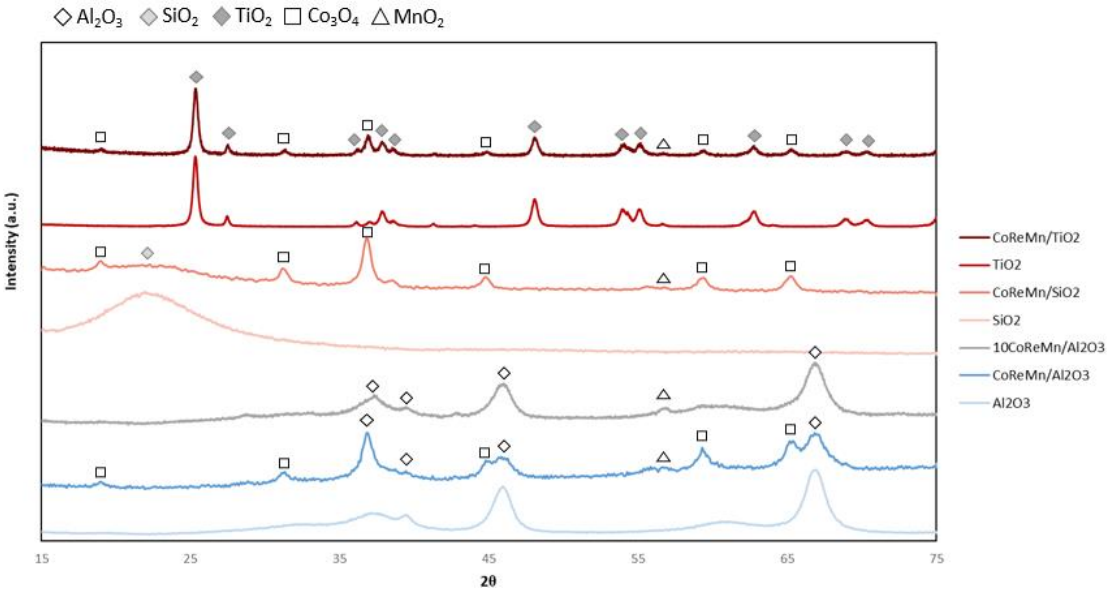

Figure 4.2. XRD diffractograms of supports and fresh CoReMn/Al_2O_3, 10CoReMn/Al_2O_3 CoReMn/SiO_2 and CoReMn/TiO_2 catalysts

Figure 4.3 below shows the adsorption isotherms obtained after H_2 chemisorption analysis. The results related to dispersion and particle size are shown in Table 4.2, where they are also compared with the dispersion and crystal size obtained with XRD.

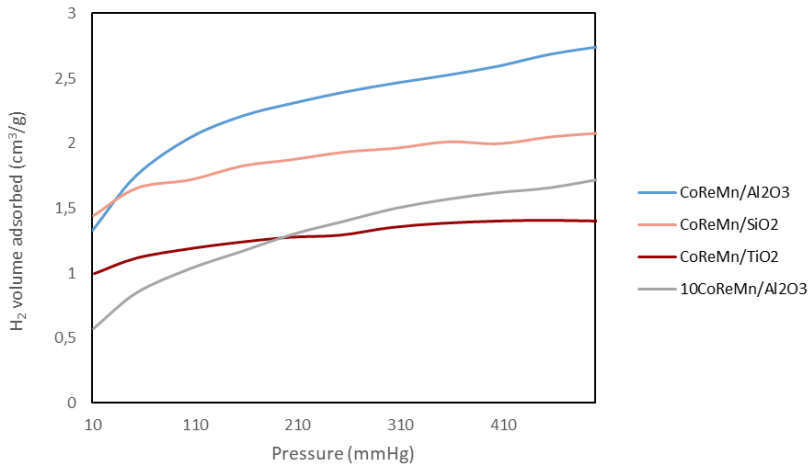

Figure 4.3. Adsorption isotherms by H_2 chemisorption of fresh CoReMn/Al_2O_3, 10CoReMn/Al_2O_3 CoReMn/SiO_2 and CoReMn/TiO_2 catalysts

The catalyst supported by silica has the highest dispersion with a 6.0 %, followed by those supported by alumina (5.6 %) and titania (3.6 %). It is reasonable, as its larger surface area permits the formation of smaller particles. The difference in particle size between $CoReMn/Al_2O_3$ and $CoReMn/SiO_2$ is negligible, whereas $CoReMn/TiO_2$ particles are substantially larger. A difference in dispersion and particle size can also be observed between the two catalysts supported on alumina. When the cobalt loading goes from 15 to 10% the dispersion drops from 5.6 to 3.2% and the particle size nearly doubles. This result could be expected because the calculation of dispersion assumed 10% cobalt, but part of the cobalt will be incorporated into the spinel lattice of the alumina, so the estimation may not be accurate. To fully understand the right dispersion value, it is necessary to calculate the degree of reduction. On the other hand, the particle size measured in chemisorption includes the cobalt alloys with the support, which is not active. For the same reason it is correct to compare it with the crystallite size obtained by XRD to a certain extent, because in this case the measurement refers to the various phases of the metal. It is noticeable that the dispersion value obtained by XRD is higher for all the cases, compared with the value obtained by H_2 chemisorption. This might be attributed, as mentioned before, to the formation of non-reducible cobalt species, which will be affect the calculated particle size. In the case of $10CoReMn/Al_2O_3$, it was not possible to obtain the crystal size of Co_3O_4 since the peak was not visible in its diffractogram.

Table 4.2. Dispersion, particle size and crystal size of fresh $CoReMn/Al_2O_3$, $10CoReMn/Al_2O_3$ $CoReMn/SiO_2$ and $CoReMn/TiO_2$ catalysts by H_2 chemisorption and XRD

Catalyst	Chemisorption		XRD	
	D_{chem} (%)	d_p (nm)	D_{XRD} (%)	d_c (nm)
$CoReMnAl_2O_3$	5.6	17.0	7.9	12.2
$10CoReMnAl_2O_3$	3.2	30.0	-	-
$CoReMn/SiO_2$	6.0	16.0	10.0	12.8
$CoReMn/TiO_2$	3.6	26.5	4.0	24.3

Finally, Figure 4.4 below shows the patterns obtained by TPR for the 4 fresh catalysts. Cobalt oxide follows a two-step reduction to cobalt (Equations 2.24-25), thus

the TPR profile is expected to have 2 peaks. The first one is attributed to the reduction of Co_3O_4 to CoO and the second one to reduce CoO to Co. However, $CoReMn/Al_2O_3$ and $10CoReMn/Al_2O_3$ profiles show 3 different peaks. The first is attributable to precursor nitrate residues remaining after calcination. The other two peaks are associated with the reduction of Co^{+3} (Co_3O_4) to Co^{+2} (CoO) and Co^{+2} to Co^0 (metallic Co), respectively. Moreover, these three peaks are shifted to the right in the $10CoReMn/Al_2O_3$ catalysts. From previous research [45] it can be assumed that as cobalt loading increases, both the reducibility and its H_2 consumption capacity are enhanced. Regarding $CoReMn/SiO_2$ and $CoReMn/TiO_2$, only the peaks associated with the reduction of Co_3O_4 to CoO and CoO to Co are observed. Their temperatures are also a little bit shifted comparing with the cobalt supported on alumina, but in general the profiles are very similar.

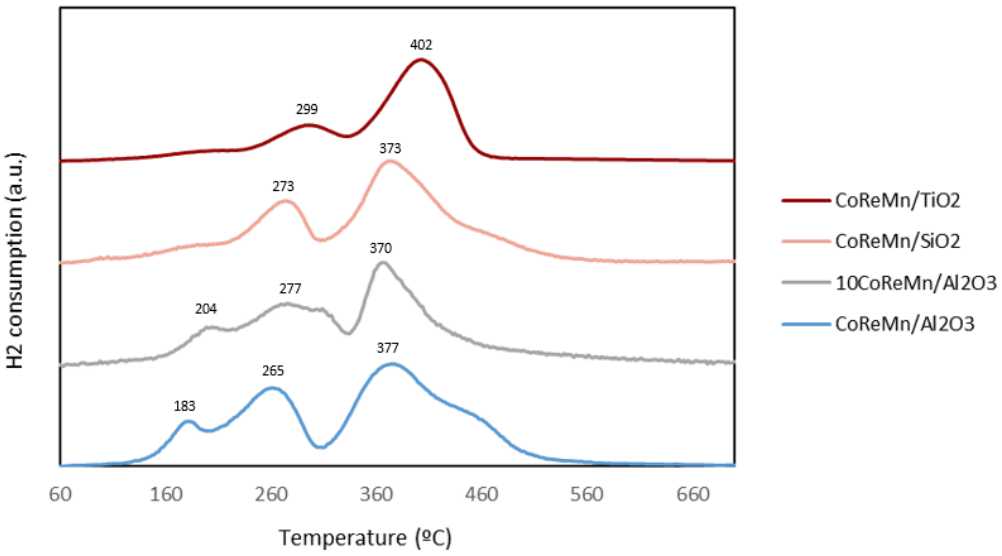

Figure 4.4. TPR profiles of fresh $CoReMn/Al_2O_3$, $10CoReMn/Al_2O_3$ $CoReMn/SiO_2$ and $CoReMn/TiO_2$ catalysts

4.2 Effect of the potassium in different salts

The first set of experiments consist of testing the $CoReMn/Al_2O_3$ catalyst with different solutions of potassium and the results can be found in Appendix B. They showed a progressive decrease in the initial activity, suggesting that the setup is being contaminated by potassium after every experiment. Despite the setup was exhaustively cleaned after every test, cross-contamination between experiments is still possible.

The second set of experiments consist of testing the same catalyst, $CoReMn/Al_2O_3$ with KNO_3, KCl, K_2SO_4 and water, to have a reference. Results are represented in the Figure 4.5. The catalyst activity during the course of the reaction was determined in terms of CO conversion for 35 hours on stream (hoS). It was measured while poisoned with KNO_3 (light blue graph), KCl (grey graph), K_2SO_4 (yellow graph) and water (orange graph). The first addition of the salts was performed after 8 hours of reaction with a concentration of 70 ppm. All of them have a volume of 8 mL and were added at a rate of 2 mL/h; therefore, for 4 hours the activity of the poisoned catalyst is being measured. The second addition consists of 700 ppm solutions and is performed after 24 hours of reaction, with the same conditions as the first one.

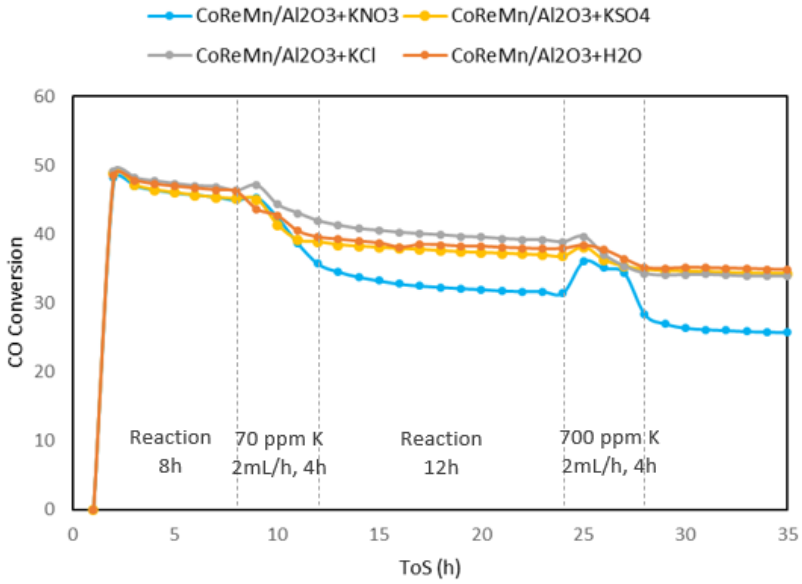

Figure 4.5. Activity in terms of CO conversion at 240 °C, 5 bar, 15 $L/g_{cat}·h$ of $CoReMn/Al_2O_3$ posioned with KNO_3, KCl, K_2SO_4 and water (additions at 2 mL/h)

During the first addition, a very similar behaviour can be observed in all cases except in the case of nitrate, which reduced the activity significantly more compared with the other salts. Chloride and sulphate solutions behave practically the same in all cases as water, which is surprising since sulphur is also known as a potential contaminant for cobalt [6]. As for the chloride solution, KCl had been reported previously to its weak effect over the cobalt-based catalysts [20]. This deactivation might be attributed to the increase of partial pressure of water in the system and not to the poisoning of the catalysts with K, since some studies [73, 74], claim that water can cause the re-oxidation

of the cobalt particles and therefore, its deactivation. Furthermore, this oxidation is strongly dependant on the partial pressure of water.

The different behaviour when the catalyst is poisoned with KNO_3 could be explained by the recombination of the K^+ with their respective anions inside the reactor in the case of KCl and K_2SO_4, hindering the reaction of K with the cobalt catalysts. Also, the physical properties of KNO_3, KCl and K_2SO_4 could be influencing, since KCl and K_2SO_4 have similar melting and boiling points, but KNO_3 differs significantly, as shown in Table 4.3:

Table 4.3. Melting and boiling points of the K-salts: KNO_3, KCl and K_2SO_4

K-Salt	Melting point (°C)	Boiling point (°C)
KNO_3	334	400
KCl	770	1420
K_2SO_4	1069	1689

During the second addition of K, the behaviour between the KNO_3 and the other experiments was noticeable different. In the case of H_2O, KCl and K_2SO_4, there is also a soft increase once the solution starts to be added, but it is mainly associated with the effect of water. From previous research [12,22,58], the decrease in activity after the addition of potassium and water was expected. On the case of KNO_3, there is a significant increase during the addition of the solution. This increase may be due to the selective catalytic reduction of NO_x species formed from the KNO_3 to N_2 by CO (CO-SCR) [75]. Considering that the N_2 is used in the experiment as internal standard, the increase in N_2, due to the reduction of NO_x species, could affect the calculation of CO conversion, resulting in an increase in CO conversion. If consider that all NO_x is reducing to N_2, the addition of 700 ppm of KNO_3, corresponds to an increase of N_2 from 7.5 mL/min to 7.8 mL/min. On the other hand, the measurement of the N_2 area in the TCD increased around 60 μV·s. This increase in the TCD corresponds to an increase in N_2 of 0.32 mL/min, similar value than the calculated. Therefore, the increase in activity might be due to this NO_x reduction.

There are two different assumptions that can be drawn from these first experiments. First, maybe the reason why the activity is suffering an important drop until an apparent maximum is because the potassium is blocking specific active sites in the cobalt surface. Once they are occupied, the effects on activity are irreversible and continue addition of more potassium has no further effect. On the other hand, it could be possible that the potassium is not passing completely through the entire catalyst bed, so it only remains in the upper layers, and it is not reaching all the active sites.

Besides, the Figure 4.6 represents the selectivity profiles towards CH_4, C_{5+} products, CO_2, and C_{2-4} olefins while poisoned with KNO_3 (light blue graph), KCl (grey graph), K_2SO_4 (yellow graph) and water (orange graph).

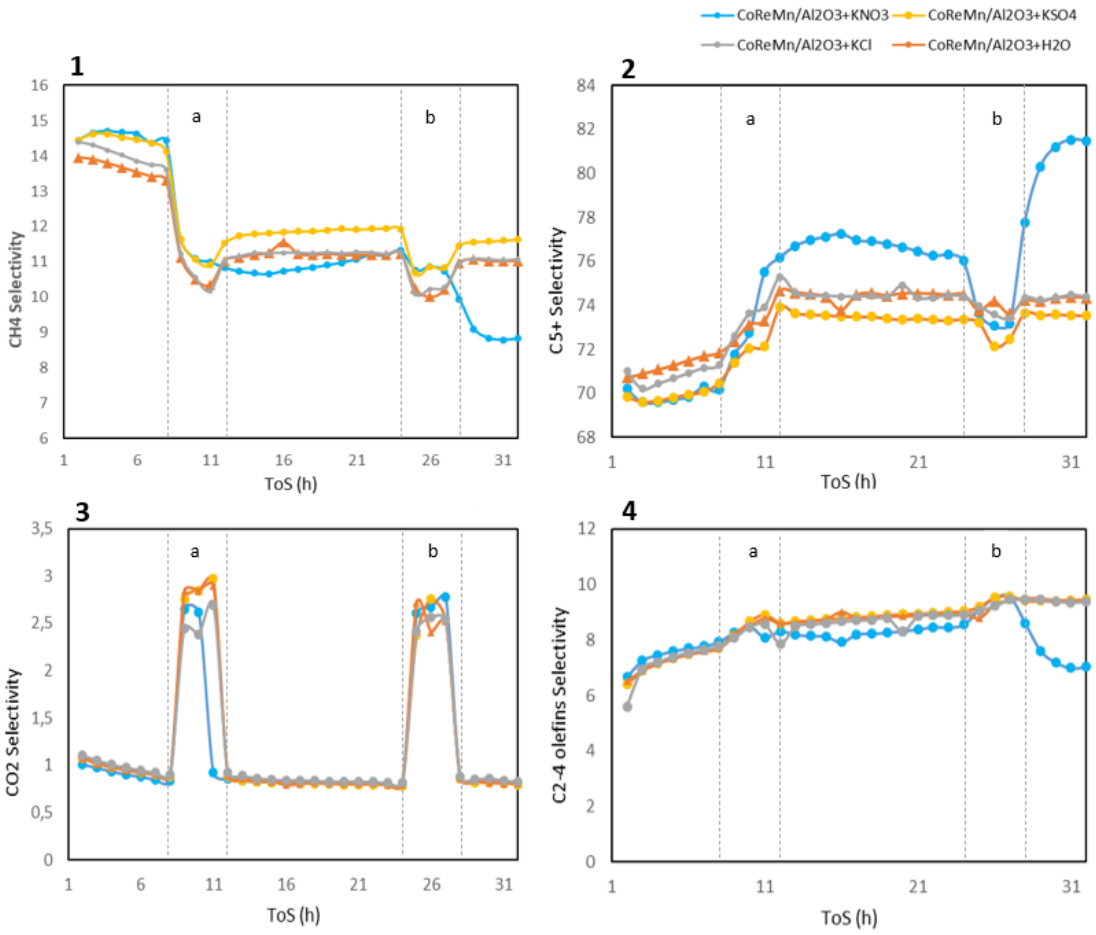

Figure 4.6. CoReMn/Al_2O_3 selectivity at 240 °C, 5 bar, 15 L/g_{cat}·h towards (1) CH_4, (2) C_{5+} products, (3) CO_2 and (4) C_{2-4} olefins; (a) Addition of 70 ppm KNO_3, KCl, K_2SO_4, water at 2 mL/h (b) Addition of 700 ppm KNO_3, KCl, K_2SO4, water at 2 mL/h

As expected from previous research [12,22], the addition of potassium implies a decrease in selectivity towards methane and increases in C_{5+}. The CO_2 graph shows that the solution is entering in the system, since the introduction of water favours the water gas shift reaction (Equation 2.6). Once again, nitrate is the salt that has the greatest effect. But in general, in the four profiles the first addition of solution results in the sudden drop in methane and increase in C_{5+}. Once the solution is completely added the selectivity tends to return to the same level but remains lower in methane and higher in C_{5+} than initially. During the second addition, the same effect occurs but this time it is only nitrate that continues decreasing methane and increasing C_{5+}, the rest remains in the same level as before.

The Figure 4.7 below represents in more detail the changes in CH_4, C_{5+} products, CO_2, and C_{2-4} olefins selectivity after each addition of KNO_3.

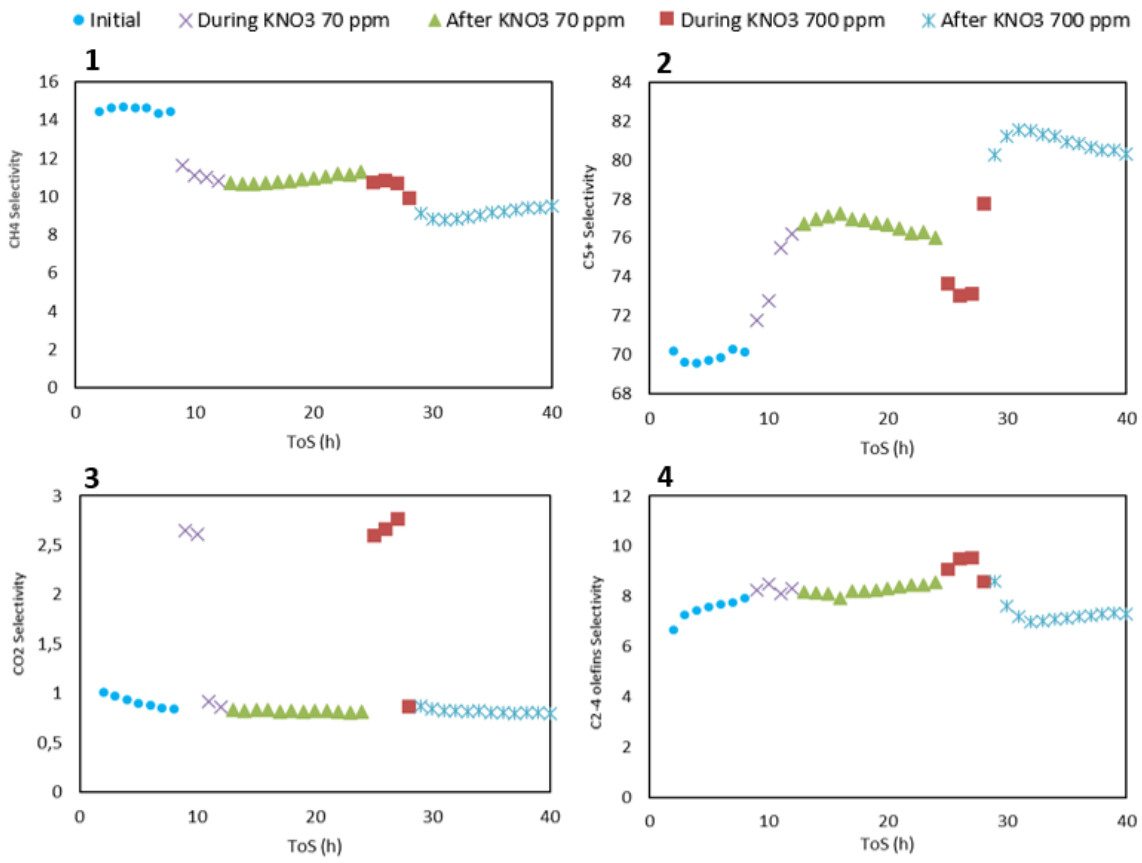

Figure 4.7. CoReMn/Al_2O_3 selectivity at 240 °C, 5 bar, 15 L/g_{cat}·h towards (1) CH_4, (2) C_{5+} products, (3) CO_2 and (4) C_{2-4} olefins when poisoned with KNO_3 (addition at 2 mL/h)

It can be observed how during the addition of the solutions the activity changes drastically. After the addition of KNO_3 700 ppm the selectivity towards methane and C_{5+} reaches its lowest and highest value, respectively. However, it is observed that as time advances on stream, it tends to return slowly to its initial values. Therefore, once the dissolution is added the potassium effect is not as strong as during addition. Potassium is very mobile under FTS conditions, according to previous research [12], so this could be one reason why selectivity changes once potassium is not entering into the system. In the case of C_{2-4} alpha-olefins, the behaviour with the potassium is difficult to explain, remaining fairly stable through the experiment, except for a decrease after the second addition of K.

4.3 Effect of the concentration of potassium

To test the first hypothesis, if there is a maximum level of poisoning, another type of experiments was tried. $CoReMn/Al_2O_3$ was tested with a higher concentration of KNO_3 from the first addition in order to confirm if the activity could decrease more than a certain level. The activity behaviour is reflected in the dark blue graph in Figure 4.8.

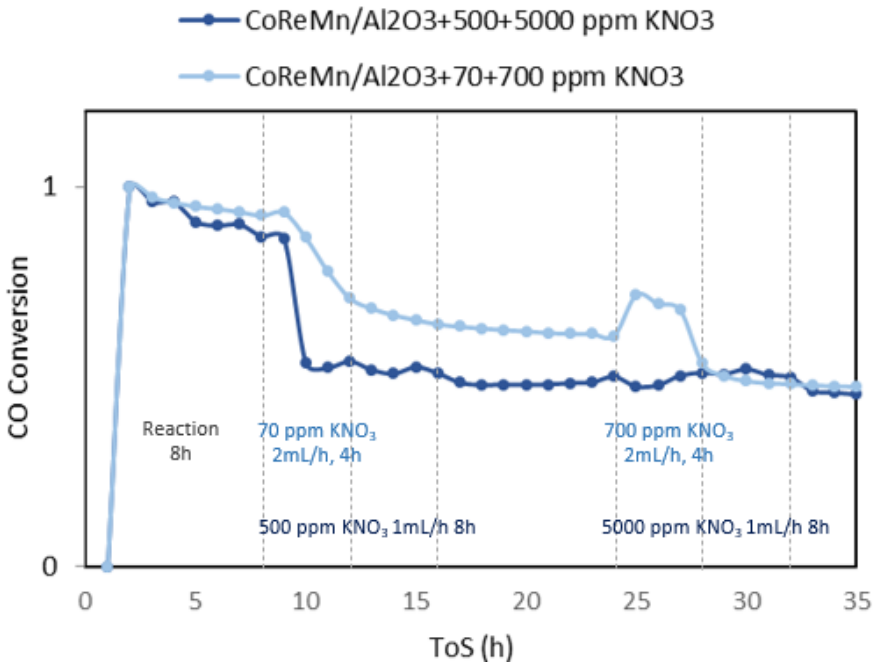

Figure 4.8. Activity in terms of CO conversion at 240 °C, 5 bar, 15 L/g_{cat}·h of $CoReMn/Al_2O_3$ posioned with different concentrations of KNO_3: 500 + 5000 ppm at 1 mL/h and 70 + 700 ppm at 2 mL/h

After 8 hours of reaction 8 mL of 500 ppm KNO_3 solution is added at 1 mL/hour. Therefore, this time the activity during the poisoning of the catalyst is evaluated over a period of 8 hours. After 24 hours the second solution is added with a higher concentration of 5000 ppm and the same conditions as the first one. Its activity is being compared with the previous experiment with KNO_3 (light blue graph), where 70 and 700 ppm KNO_3 solutions were added after 8 and 24 hours, respectively, at 2 mL/h. Considering the results, it seems that with a higher concentration the active sites are completely blocked from the beginning, since when adding again a higher concentration (5000 ppm) after 24 hours of reaction there is no visible effect. Moreover, in both experiments the same level of activity is reached, suggesting that certain types of active sites are completely blocked. Consequently, it can be assumed that at lower concentrations there are still active sites that have not yet been blocked. However, it is challenging to determine with certainty the minimum potassium concentration required to completely poison these active sites. Furthermore, it can be assumed that the partial pressure of the water at the reactor inlet could be also influencing the activity behaviour.

Regarding selectivity, Figure 4.9 below shows the differences between both experiments in the selectivity towards CH_4, C_{5+} products, CO_2, and C_{2-4} olefins while poisoned with 500 and 500 ppm KNO_3 (dark blue graph) and 70 and 700 ppm of KNO_3 solution (light blue graph). The conclusion is not very clear because so many variables are involved, but in any case, the selectivity reaches the same point in both experiments after the two additions (after 16 and 32 hours on stream), indicating that the concentration may not substantially affect the selectivity, but it does affect the activity. It can be observed that the rate of addition of the solutions does slightly affect the profiles. In the case of methane, during the second addition of KNO_3 5000 ppm (dark blue graph) the selectivity continues to increase progressively to drop sharply once the solution is completely added. On the contrary, when the rate is 2 mL/h and the 700 ppm KNO_3 solution is added (light blue graph) the drop in selectivity occurs more smoothly and progressively. Something similar occurs with the C_{5+} products. When the second solution of 5000 ppm KNO_3 is added, the selectivity increases abruptly (dark blue graph) instead of increasing gradually (light blue graph).

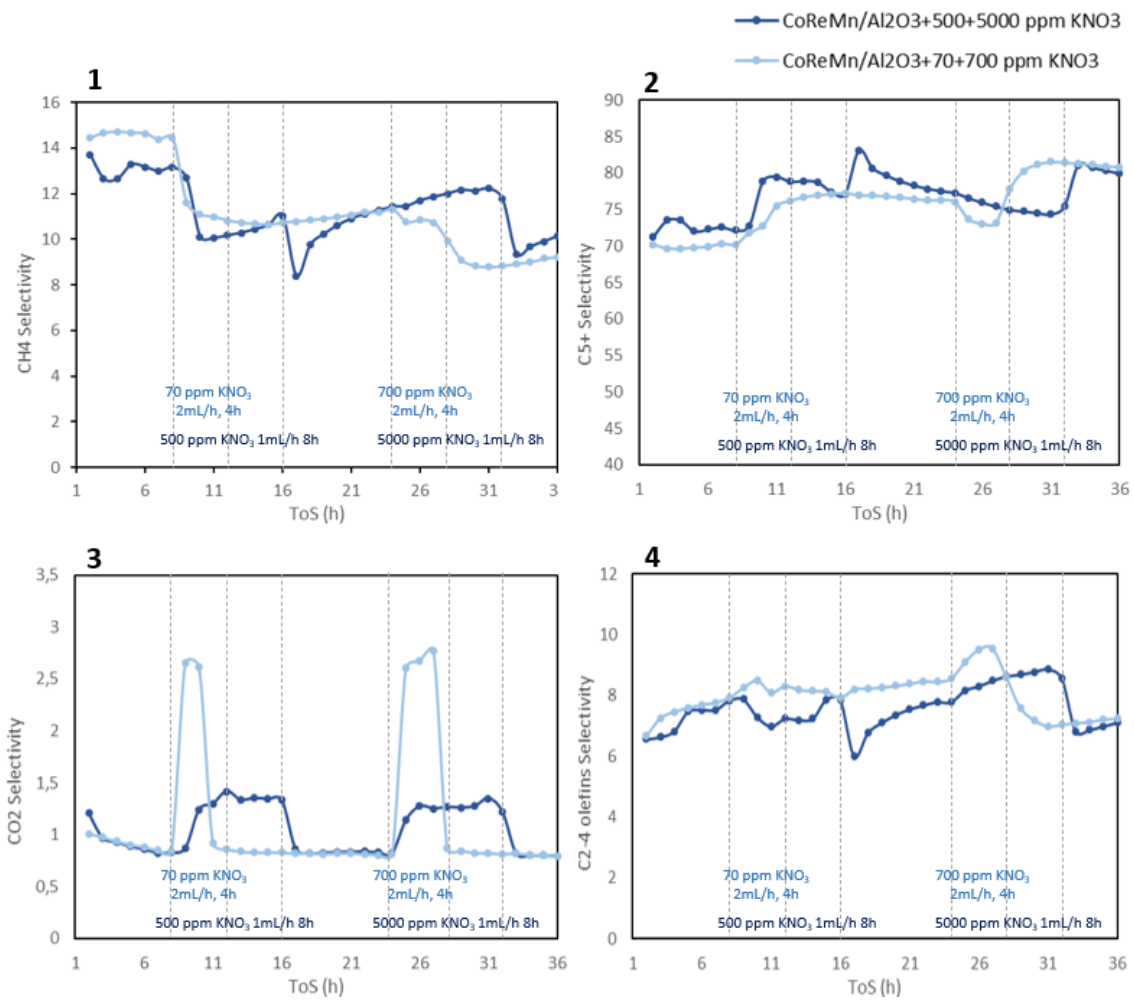

Figure 4.9. CoReMn/Al_2O_3 selectivity at 240 °C, 5 bar, 15 L/g_{cat}·h towards (1) CH_4, (2) C_{5+} products, (3) CO_2 and (4) C_{2-4} olefins when poisoned with different concentrations of KNO_3: 500 + 500 ppm at 1 mL/h and 70 + 700 ppm at 2 mL/h

The same experiment was repeated with a potassium salt whose effect on activity was less pronounced in previous experiments. For this purpose, a 700 ppm solution of KCl was introduced after 8 hours of reaction at 2 mL/h. The result is represented by the red curve in Figure 4.10. It is being compared with the first experiment that was performed with KCl on this same catalyst (blue graph), where 70 and 700 ppm KNO_3 solutions were added after 8 and 24 hours, respectively, at 2 mL/h. The addition rate is in both cases 2 mL/h. There are no big differences between the two profiles. It might be expected that with a higher concentration of potassium chloride the activity would drop to a lower level since the beginning. However, approximately the same activity level is reached after 22 hours on stream and an increase in activity during the addition of the solution is again observed. In this case the addition rate is the same

in both experiments so perhaps the concentration is the influencing factor in this rise. In any case, the same trend is followed in both cases, suggesting that the concentration has a low impact on salts with a weaker effect on activity.

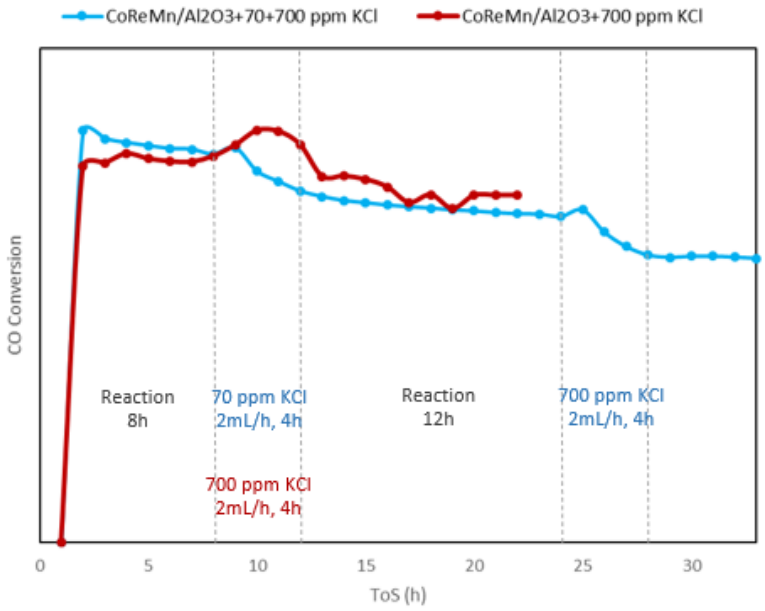

Figure 4.10. Activity in terms of CO conversion at 240 °C, 5 bar, 15 L/g_{cat}·h of CoReMn/Al_2O_3 poisoned with different concentrations of KCl (additions at 2 mL/h)

The effect on selectivity is negligible between both experiments. The selectivity profiles towards CH_4, C_{5+}, CO_2 and C_{2-4} olefins obtained from both experiments can be found in Appendix B.

4.4 Effect of the support

In order to test if the surface characteristics of the support played a role in the poisoning of the catalyst, the same test with KNO_3 was performed with cobalt supported on different materials: Al_2O_3, SiO_2 and TiO_2.

Figure 4.11 below represents the activity profiles of CoReMn/Al_2O_3 (blue graph), CoReMn/SiO_2 (pink graph), and CoReMn/TiO_2 (red graph), when they are poisoned with a solution of KNO_3 of 70 ppm after 8 hours of reaction and another of 700 ppm after 24. All solutions are added at a rate of 2 mL/h. The behaviour in activities is same as observed in previous experiments: after the first addition the activity decreases considerably, especially in the case of titania. During the second addition an increase in

activity appears again and returns to the original level once the addition is completed. Titania has larger particle size, so it may also be a factor in determining the number of active sites that can be occupied by potassium. We could also think that the interaction of potassium with the support is different in the 3 cases and that is why these differences are found. In any case, the catalyst supported on titania seems to be more prone to K poisoning in these conditions than with alumina and silica.

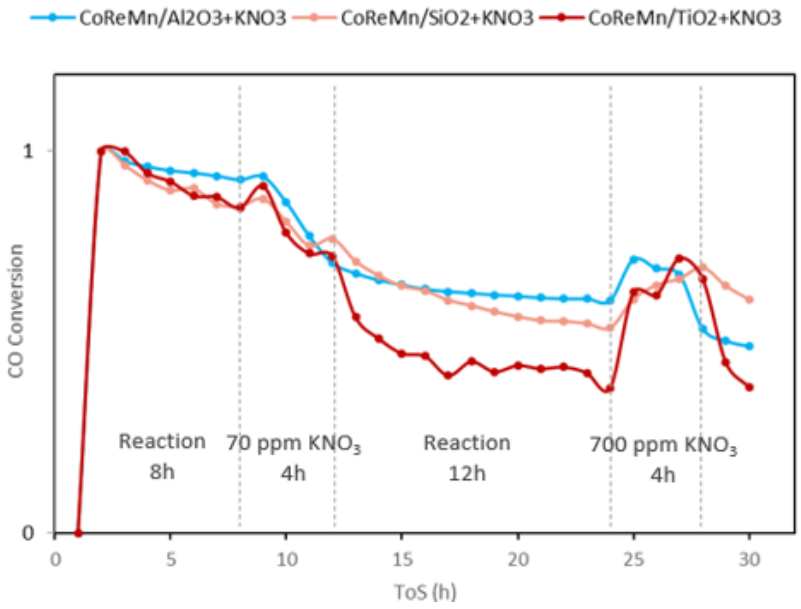

Figure 4.11. Activity in terms of CO conversion at 240 °C, 5 bar, 15 L/g_{cat}·h of CoReMn/Al_2O_3, CoReMn/SiO_2 and CoReMn/TiO_2 poisoned with KNO_3 (additions at 2 mL/h)

The selectivity of these three catalysts towards methane and C_{5+} is shown in Table 4.4 and 4.5, respectively. Drop in methane and increase in C_{5+} products can be observed once again. During the addition of KNO_3 70 ppm the first drop of selectivity in methane and increase in C_{5+} occurs in all three cases, although significantly lower in the case of CoReMn/TiO_2. However, it can be observed that the selectivity is always affected mainly during this addition of potassium, once the addition of solution is completed and after some hours after the addition, the selectivity slightly increases again in methane and decreases in C_{5+}. The same phenomenon occurs after 30 hoS, when 2 hours have already passed since the last addition of potassium, which is when the lowest and highest values are obtained. After 30 hours, when two hours have gone by since the last potassium addition, the same phenomenon occurs. However, the opposite effect occurs in the case of CoReMn/Al_2O_3, which continues decreasing CH_4 and increasing C_{5+} products.

Table 4.4. CH_4 selectivity at 240 °C, 5 bar, 15 L/g_{cat}·h in CoReMn/Al_2O_3, CoReMn/SiO_2 and CoReMn/TiO_2 when poisoned with KNO_3

	CoReMn/Al_2O_3	**CoReMn/SiO_2**	**CoReMn/TiO_2**
Before KNO_3 70 ppm (8 hoS)	14.4	9.1	12.4
After KNO_3 70 ppm (12 hoS)	10.8	6.7	12.0
Before KNO_3 700 ppm (24 hoS)	11.3	9.7	13.6
After KNO_3 700 ppm (28 hoS)	9.9	6.6	10.7
After 30 hoS	8.8	7.7	10.2

Table 4.5. C_{5+} selectivity at 240 °C, 5 bar, 15 L/g_{cat}·h in CoReMn/Al_2O_3, CoReMn/SiO_2 and CoReMn/TiO_2 when poisoned with KNO_3

	CoReMn/Al_2O_3	**CoReMn/SiO_2**	**CoReMn/TiO_2**
Before KNO_3 70 ppm (8 hoS)	70.2	76.9	73.6
After KNO_3 70 ppm (12 hoS)	76.2	80.9	73.9
Before KNO_3 700 ppm (24 hoS)	76.0	75.7	73.1
After KNO_3 700 ppm (28 hoS)	77.8	81.3	76.0
After 30 hOs	81.2	79.8	75.5

The Figure 4.12 below represents the behaviour in the activity of these three catalysts when they are poisoned (continuous curve) with potassium and when they are not (discontinuous curve). After 24 hours on stream a clear difference between both activities is observed, confirming once again that the addition of potassium to the system could be the reason of this immediate negative effect.

The selectivity profiles towards CH_4, C_{5+}, CO_2 and C_{2-4} olefins of the CoReMn/Al_2O_3, CoReMn/SiO_2 and CoReMn/TiO_2 catalysts when poisoned and when they are not can be found in Appendix B.

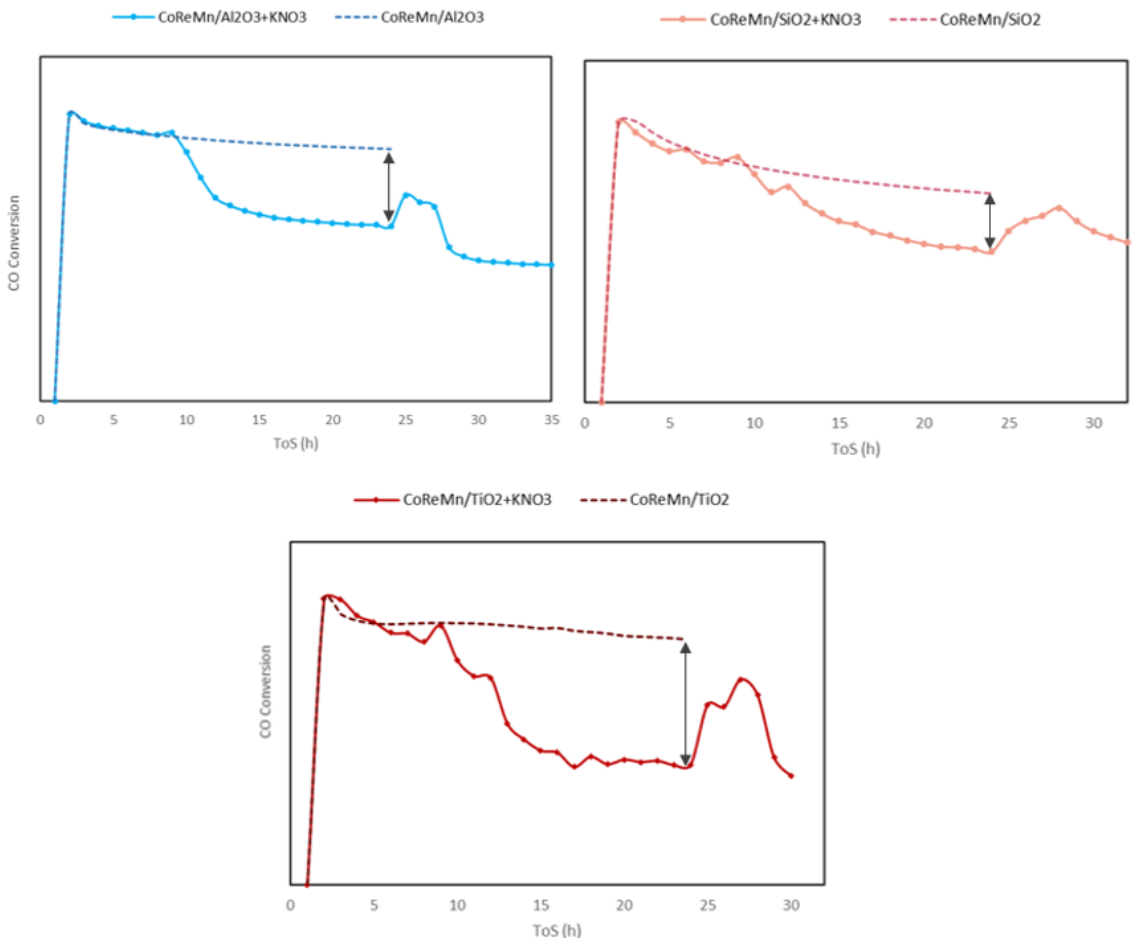

Figure 4.12. Differences in activity at 240 °C, 5 bar, 15 L/g_{cat}·h when CoReMn/Al_2O_3, CoReMn/SiO_2 and CoReMn/TiO_2 catalysts are poisoned with KNO_3 and when they are not.

4.5 Effect of the cobalt loading

The effect of potassium was also tested as a function of cobalt loading on the catalyst. Therefore, the same type of experiment was performed on the 10CoReMn/Al_2O_3 catalyst with 10% cobalt, and the result is shown by the grey graph in Figure 4.13, where it is being compared with the CoReMn/Al_2O_3 catalyst tested with 15% cobalt (blue graph).

In the reaction with the lower cobalt loading catalyst, the space velocity was modified. It was decreased from 250 mL/h (15 L/g_{cat}·h) of syngas to 140 mL/h (12 L/g_{cat}·h) to try to increase the conversion, since the 10% catalyst is expected to be less active. It can be observed the activity of both catalysts during 31 hours on stream in terms of CO conversion. After 8 hours the 70 ppm KNO_3 solution is added ad 2 mL/h, that is when the activity suffers the greater drop. After 24 hours on stream, the second

solution of 700 ppm KNO_3 is added with the same conditions as the first one, that is when the activity decreases a bit to go back to the normal activity level as before the addition. It suffers again a decrease, but it is not as significant as it was after the first addition.

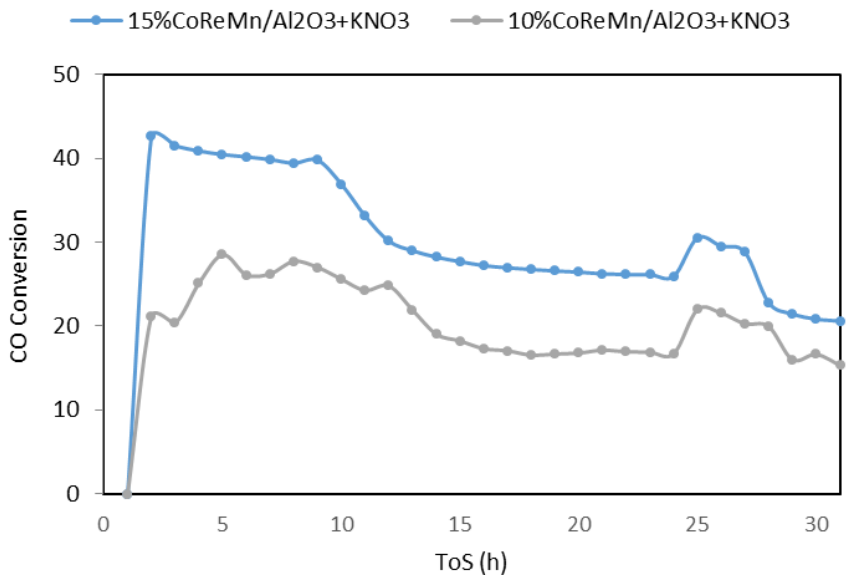

Figure 4.13. Activity in terms of CO conversion at 240 °C, 5 bar, 15 and 12 L/g_{cat}·h of CoReMn/Al_2O_3 and 10CoReMn/Al_2O_3 when poisoned with KNO_3 (additions at 2 mL/h)

In order to compare both activities more accurately, the following Figure 4.14 shows the unitarian activity of these two catalysts.

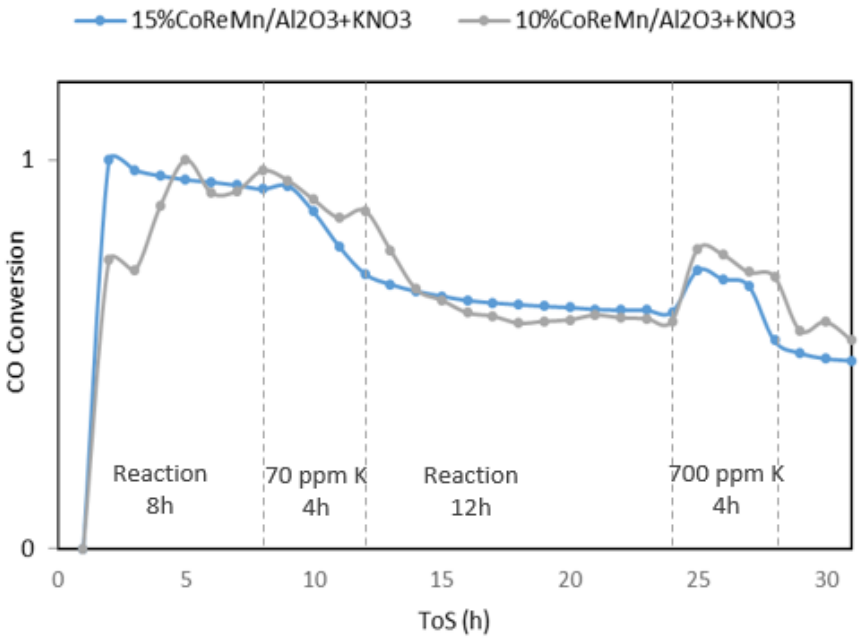

Figure 4.14. Unitarian activity at 240 °C, 5 bar, 15 and 12 L/g_{cat}·h of CoReMn/Al_2O_3 and 10CoReMn/Al_2O_3 when posioned with KNO_3 (additions at 2 mL/h)

As can be seen, potassium does not act differently depending on the amount of cobalt in the material, since the same activity profile is obtained. Therefore, impregnating a greater or lesser quantity of the precursor metal into the catalyst alters its activity, but the dynamics of potassium poisoning remain unaltered.

Using the same catalyst, we intended to test the second of the initial assumptions. There is still a chance that the potassium solution is not completely passing through the catalyst bed and is instead remaining in the uppermost layers, preventing it from reaching all the active sites in the metal. Therefore, in order to determine if the SiC mixed with the catalysts is affecting its permeability, the bed distribution was modified: 15 g of SiC were placed at the bottom of the reactor and the remaining 4 g were mixed with 1 g of catalyst at the top of the reactor. The same experiment was performed as previously, reflected in the dark graph in Figure 4.15. Once again, the behaviour is the same after the potassium additions, so it seems that the dilution with SiC does not influence strongly over the activity. Nevertheless, After the reaction, it was much easier to separate from the cobalt. This is an important advantage since it allows for easier characterization after the reaction.

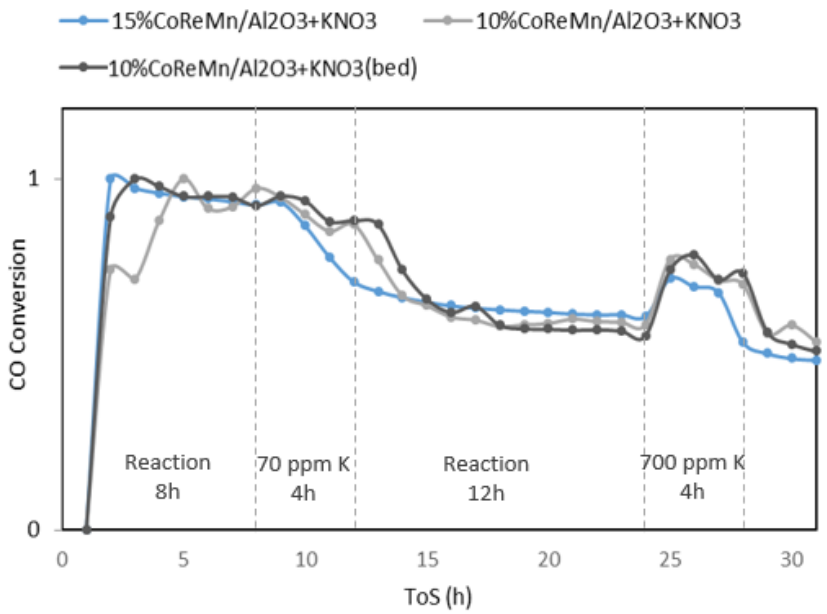

Figure 4.15. Activity of $CoReMn/Al_2O_3$ and $10CoReMn/Al_2O_3$ at 240 °C, 5 bar,15 and 12 $L/g_{cat}{\cdot}h$ when posioned with KNO_3 and different catalyst bed distribution (additions at 2 mL/h)

The following Tables 4.6 and 4.7 represent the selectivity towards CH_4 and C_{5+} products, respectively, achieved with the $CoReMn/Al_2O_3$ and $10CoReMn/Al_2O_3$ catalysts

when they are poisoned with KNO_3 and the one accomplished when the bed distribution is changed:

*Table 4.6. CH_4 selectivity at 240 °C, 5 bar, 15 and 12 L/g_{cat}·h in CoReMn/Al_2O_3 and 10CoReMn/Al_2O_3 when poisoned with KNO_3 (*with different bed distribution)*

	15CoReMn/Al_2O_3	**10CoReMn/Al_2O_3**	**10CoReMn/Al_2O_3***
Before KNO_3 70 ppm (8 hoS)	14.4	18.2	19.0
After KNO_3 70 ppm (12 hoS)	10.8	12.3	14.0
Before KNO_3 700 ppm (24 hoS)	11.3	14.1	15.4
After KNO_3 700 ppm (28 hoS)	9.9	14.5	11.6
After 30 hoS	8.8	11.2	10.6

*Table 4.7. C_{5+} selectivity at 240 °C, 5 bar, 15 and 12 L/g_{cat}·h in CoReMn/Al_2O_3 and 10CoReMn/Al_2O_3 when poisoned with KNO_3 (*with different bed distribution)*

	15CoReMn/Al_2O_3	**10CoReMn/Al_2O_3**	**10CoReMn/Al_2O_3***
Before KNO_3 70 ppm (8 hoS)	70.2	65.2	60.8
After KNO_3 70 ppm (12 hoS)	76.2	72.9	66.4
Before KNO_3 700 ppm (24 hoS)	76.0	75.4	68.7
After KNO_3 700 ppm (28 hoS)	77.8	69.7	71.8
After 30 hoS	81.2	73.6	81.2

In all cases again the addition of potassium causes a decrease in methane and an increase in C_{5+}. From 15% to 10% of cobalt, the selectivity towards methane increases and decreases towards C_{5+}, as expected because the first one is more active as it contains more cobalt active sites. Furthermore, based on previous studies [74], the increase in water partial pressure increases the chain growth probability. However, it can be observed that when the distribution in the bed is changed, the variation in both methane and C_{5+} is much more abrupt, so the different distribution in bed can have an effect in this sense, even though it is not visible in the activity. Moreover, in all cases the

addition of the solutions has a much stronger effect during the addition itself, since once the addition of solution is completed and 12 hours have gone by the selectivity slightly increases again in methane and decreases in C_{5+}, same effect as could be seen in previous experiments (Tables 4.4 and 4.5). It does not occur when the second solution has been added and the reaction is let to take place for a further 2 hours with the catalyst poisoned (After 30 hoS of global reaction). At this point the selectivity in methane reaches the lowest value and the highest in C_{5+}.

4.6 Characterization post Fischer-Tropsch synthesis

All catalysts were separated from the SiC after each experiment and analysed by X-Ray Diffraction just to verify that potassium was entering the system, and the changes in activity and selectivity could actually be due to its presence. The following Figure 4.16 represents the XRD pattern of the spent catalysts poisoned with KNO_3, KCl, K_2SO_4 and water. The structure of the fresh catalyst, that is, before the reaction, can also be observed.

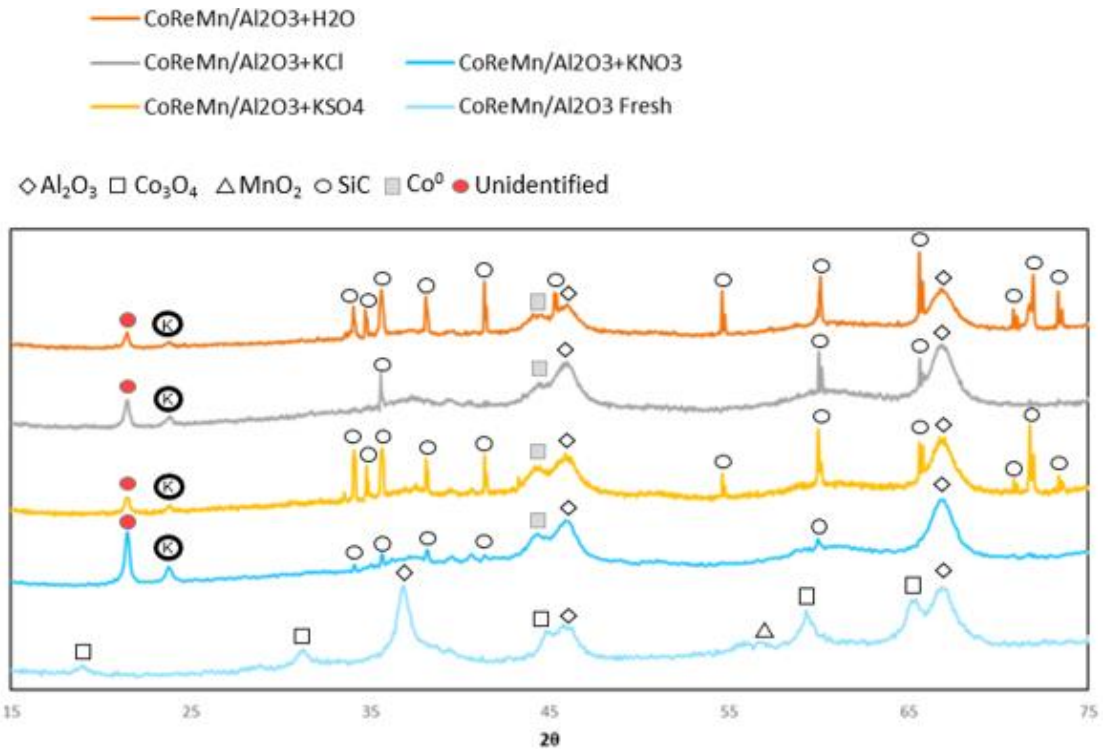

Figure 4.16. XRD diffractogram of fresh CoReMn/Al_2O_3 and when poisoned with KNO_3, KCl, K_2SO_4 and water.

A small signal could be found in all cases around 24°, which could be associated with potassium species, most likely KOH or K_2O since the K^+ ion once it enters the reactor could tend to recombine with hydrogen or oxygen. Still with these patterns it is difficult to confirm that potassium species are penetrating the catalyst bed. It could be also being incorporated into the cobalt lattice or being amorphous species. Potassium is very mobile in FTS conditions, so it could be also highly dispersed in the support. It could also be found few signals from remaining SiC, since in some cases it is more complicated to separate it from the catalyst. That is why the analysis could be more hindered in some catalysts. The structure of the support and precursor does not suffer too many modifications, being able to find alumina in the same position as before the reaction and metallic cobalt around 44°. The manganese signal at 57° cannot be found once the catalyst is spent, so it can be either dispersed in the support or incorporated in the cobalt oxide lattice. The region between 34 and 44° is composed of a set of several peaks, mostly related to SiC and others more complicated to analyse that may be due to the cobalt oxide and/or complex alloys of the precursor with the support. Finally, around 21° a peak appears in all cases that could not be identified but its presence is probably due to hydrocarbons associated with the waxes that cover the catalyst after the reaction. To check this assumption, the analysis of the waxes obtained after the reaction was carried out. Their XRD patterns are shown in Appendix B. However, the results do not allow us to affirm that these peaks are due to their presence.

Furthermore, Figures 4.17-19 show the XRD pattern of $CoReMn/Al_2O_3$, $CoReMn/SiO_2$ and $CoReMn/TiO_2$ when they were poisoned with KNO_3. They are also compared with the fresh catalysts and the support profile.

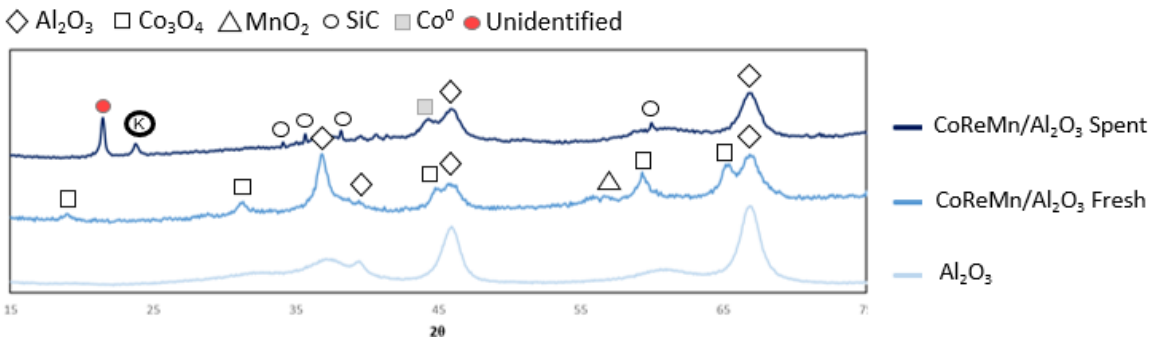

Figure 4.17. XRD diffractogram of Al_2O_3 and $CoReMn/Al_2O_3$ prior and after reaction when it is poisoned with KNO_3

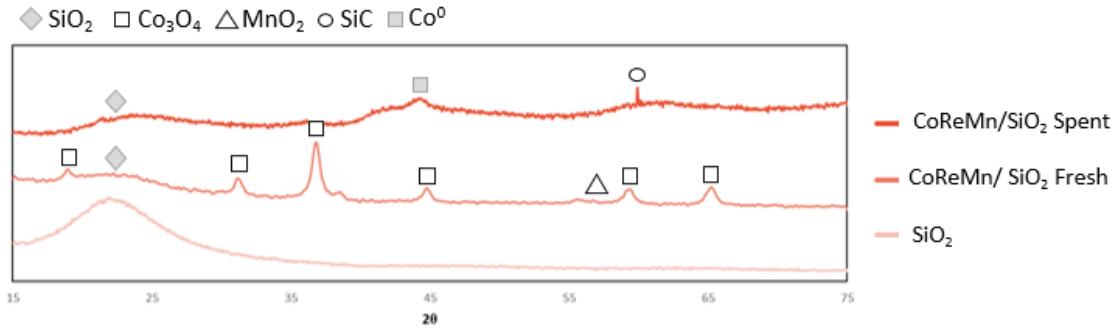

Figure 4.18. XRD diffractogram of SiO_2 and CoReMn/SiO_2 prior and after reaction when it is poisoned with KNO_3

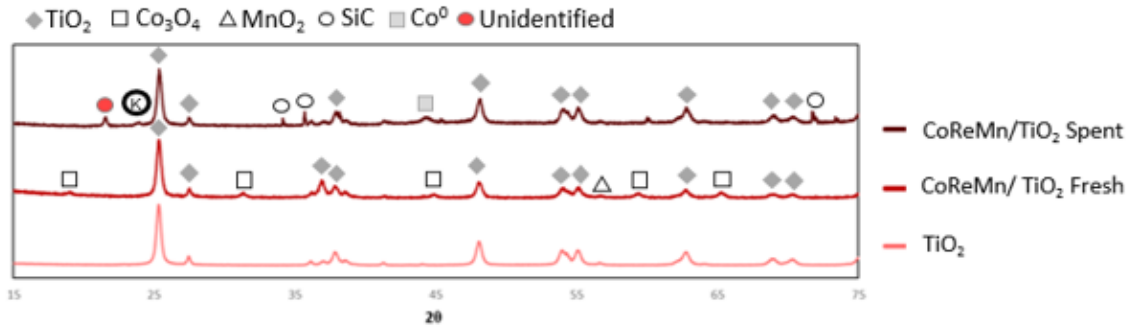

Figure 4.19. XRD diffractogram of TiO_2 and CoReMn/TiO_2 prior and after reaction when it is poisoned with KNO_3

The same signal associated with potassium as in previous analysis could be found around 24°. It is found in all cases except for CoReMn/SiO_2, whose signal may be inhibited by the characteristic SiO_2 peak. Once again, it is challenging to confirm that those peaks are associated to potassium species. Again, some peaks related with SiC could be found and peaks associated with cobalt metal and supports. Same peaks that could not be identified in previous XRD patterns appears in the CoReMn/Al_2O_3 and CoReMn/TiO_2 profiles. Once more, waxes could be hindering the analysis but no major changes in the catalyst structure could be found.

S(T)EM EDX was carried out on CoReMn/Al_2O_3 poisoned with KNO_3 and the result is shown in Figure 4.20. It can be observed that the cobalt is still well dispersed in the support as well as the manganese, even though clear agglomerations of the promoter are found. On the other hand, signal associated with potassium particles in non-preference sites was detected. Signal associated with potassium was also obtained. However, again it is difficult to confirm that potassium is truly deposited on the catalyst,

since the signal is identical to that of rhenium. The EDX results were difficult to interpret, since many peaks related with the potassium were overlapped during the analysis.

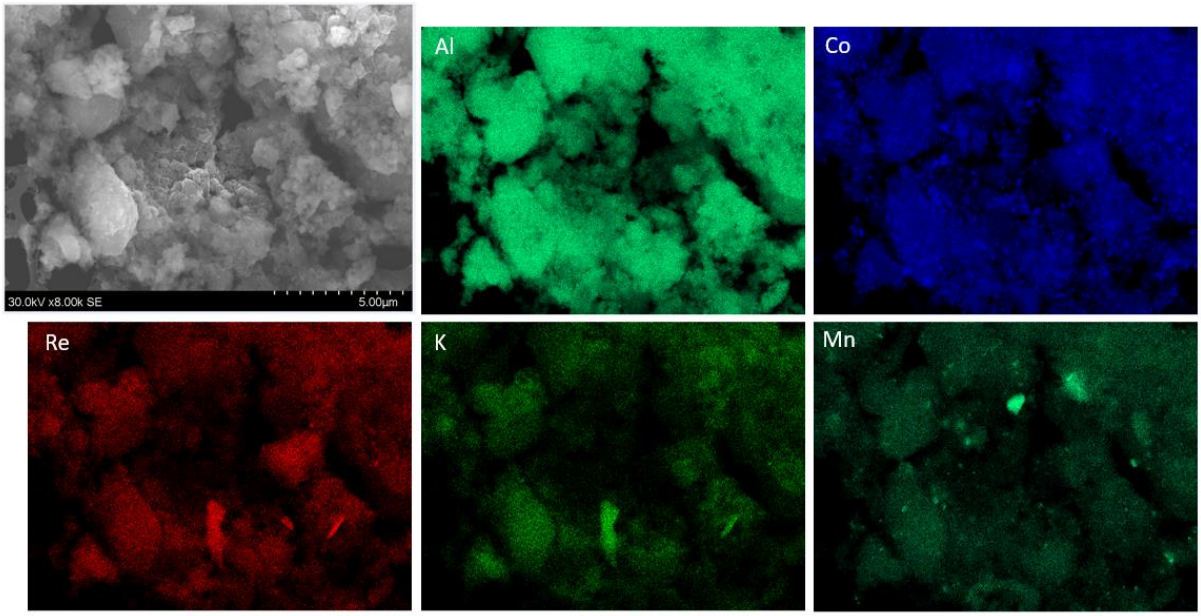

Figure 4.20. S(T)EM EDX of CoReMn/Al_2O_3 poisoned with KNO_3

XRF analysis was also performed to analyse the elemental composition of the catalyst after the reaction and it was observed that the K_2O content increased in the spent catalyst, so it is likely that these signals are actually due to potassium. The results concerning the XRF experiments are given in Appendix B.

4.6.1 Dewaxed catalysts

Removing the waxes from the catalyst makes the post-reaction analysis more realistic and reliable. Several dewaxes were performed on different catalysts as a test. The 10CoReMn/Al_2O_3 catalyst that was tested with a different bed distribution was mixed only with 4 g of SiC and after the FT reaction it was much easier to separate. Consequently, the analysis of the physical and chemical properties after FTS is based on this catalyst. The CoReMn/Al_2O_3 catalyst after testing with KNO_3 was also dewaxed and characterized, but its separation from SiC was significantly more complicated so the results are not reliable. The properties of this catalyst after dewaxing are given in Appendix B.

The following Table 4.8 shows the surface area, pore volume and pore size of 10CoReMn/Al_2O_3 before and after FT and dewaxing, obtained after BET/BJH analysis with N_2 adsorption-desorption.

Table 4.8. Surface area, pore volume and pore size of 10CoReMn/Al_2O_3 poisoned with KNO_3 obtained by BET/BJH method (fresh and dewaxed catalyst)

Catalyst	Surface area (m^2/g)	Pore volume (cm^3/g)	Pore size (nm)
Al_2O_3	185	0.74	13.4
10CoReMn/Al_2O_3 Fresh	160	0.45	12.4
10CoReMn/Al_2O_3 Dewaxed	141	0.42	12.6

As can be observed, after the reaction both the surface area and pore volume decrease but the pore size increases minimally, so sintering as a deactivation mechanism could be discarded and we could ensure once again that these changes are due to the presence of potassium in the catalyst pores. These differences can also be observed in the pore size distribution of the catalysts before and after reaction and dewax in the following Figure 4.21. The small variations from the Al_2O_3 profile may have resulted from the use of different setups in each instance.

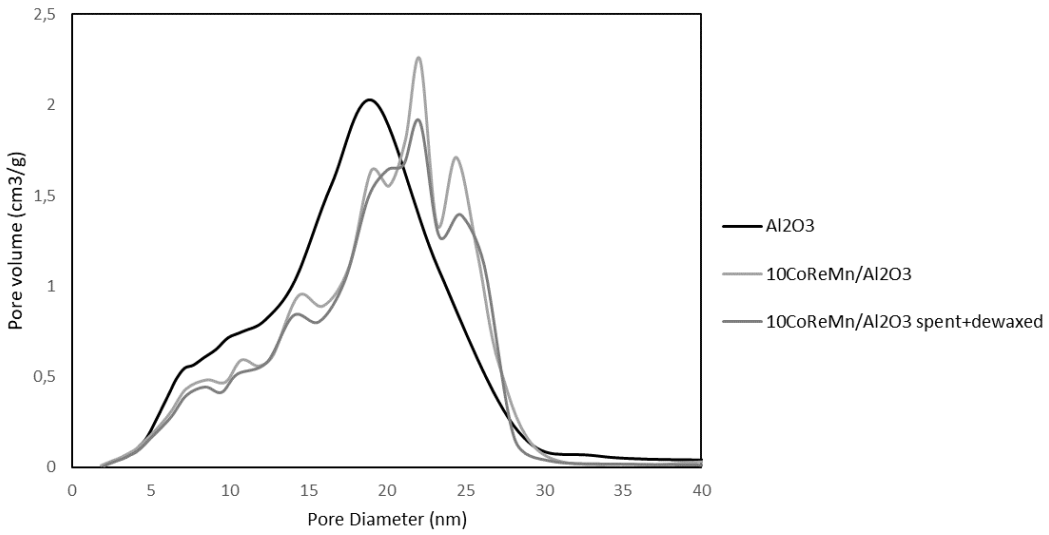

Figure 4.21. 10CoReMn/Al_2O_3 pore size distribution before and after reaction and dewaxing

The probable site blockage of potassium at the cobalt active sites is also reflected in the H_2 chemisorption results, reflected in Table 4.9 and Figure 4.22. After the reaction a small drop in dispersion and an increase in particle size can be observed, which can be explained by the inhibition of hydrogen adsorption on the surface. Once again, it would be necessary to calculate the degree of reduction, since the calculation for the

dispersion assumed 10% of cobalt, but part of this is incorporated into the spinel lattice of the alumina.

Table 4.9. Dispersion and particle size of 10CoReMn/Al_2O_3 before and after reaction and dewaxed obtained by H_2 chemisorption

Catalyst	Dispersion (%)	Particle size (nm)
10CoReMn/Al_2O_3 Fresh	3.2	30.0
10CoReMn/Al_2O_3 Dewaxed	2.2	43.3

In Figure 4.22 it can also be observed that there is a small variation in the adsorption isotherm profile. In the case of the poisoned catalyst the adsorption capacity decreases with the introduction of potassium solution. Although potassium poisoning has an important impact on activity, H_2 adsorption capacity is not significantly reduced. Potassium may be inhibiting the reaction between CO and H_2 at the surface by blocking some of the most active sites in the catalyst. However, there are still a substantial number of cobalt particles available.

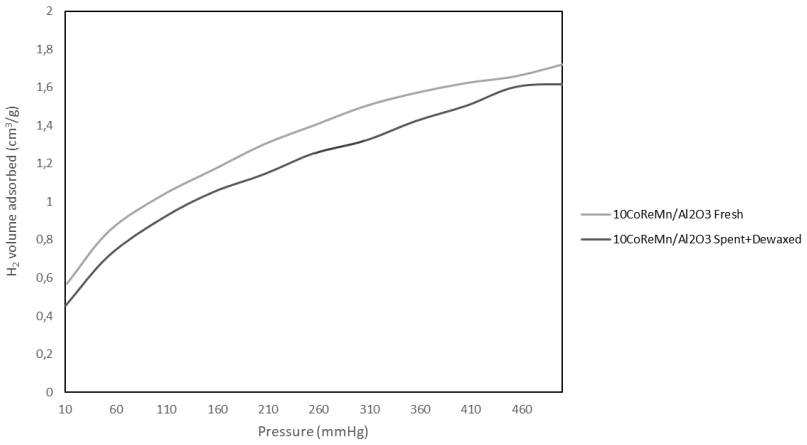

Figure 4.22. H_2 chemisorption isotherms for 10CoReMn/Al_2O_3 before and after reaction and dewax

Finally, the XRD patterns of the fresh catalyst, spent with waxes and dewaxed are shown in Figure 4.23. It can be seen that there are no significant changes in the elemental structure of the catalyst. In the spent catalyst some SiC signals are still found but considerably less than in previous analyses (Figure 4.16), which demonstrates the ease of separation by changing the bed distribution. Again, it was not possible to identify

the cobalt phases, probably because of its amorphous phase due to less cobalt loading. In this profile we also found a signal around 26° that could be associated with potassium species, but again it is challenging to confirm that assumption and identify what kind of species are present. Both this signal and the SiC ones disappear once the catalyst waxes are removed, leaving the surface cleaned.

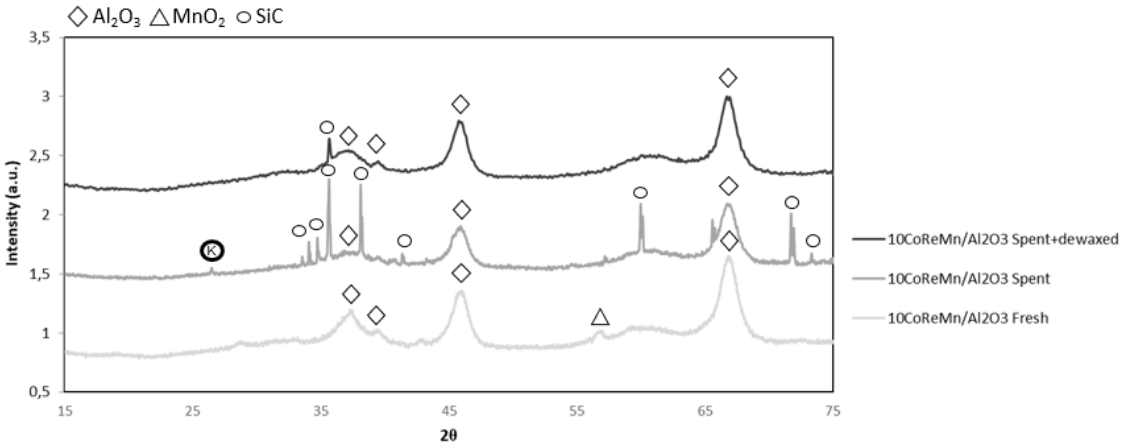

Figure 4.23. XRD diffractogram of 10CoReMn/Al_2O_3 prior to reaction, after reaction and after dewax

5 Conclusions and further work

After this work, some conclusions can be drawn. First, it is clear that potassium has a negative effect on the catalyst activity, probably by blocking specific active sites on the cobalt surface. Previous studies suggest that B5 sites could be the most affected ones, forming specific bonds with potassium and thus inhibiting the FT reaction. It has been also reaffirmed that the addition of potassium implies an increase in selectivity towards C_{5+} products and a reduction towards methane. Among the different K-salts tested as poison, KNO_3 has the greatest effect on both activity and selectivity, so side reactions with NO_3^- ions are probably taking place. On the other hand, it has been proved that the use of different support can change the activity and selectivity of the catalyst and that the one supported on titania is more prone to deactivation. The particle size of the catalyst may be then influencing the activity behaviour. On the other hand, different cobalt loading did not make the potassium act differently. The changes in activity and selectivity are supported by the observed changes in physical and chemical properties after FTS. Elemental techniques suggest that potassium is present in the catalyst bed after the reaction. Furthermore, the changes in surface area, pore volume and pore size also suggest that potassium may be deposited on the pores of the active metal.

However, it is complicated to assure what type of bonding is formed between potassium and the active metal, since previous research also suggests that potassium is very mobile under FT conditions. It is also challenging to understand what kind of side reactions are occurring once the K-salt enters the system. Currently, regeneration of the spent catalyst is being attempted in order to check if the effect caused on activity and selectivity is irreversible, or if there are some alternatives to clean the surface of the catalyst once it has come into contact with potassium. On the other hand, for further work it would be very interesting to study how Mn and Re are affecting once the solutions are introduced into the system, as there could be Mn-K and/or Re-K interactions that also influence the behaviour of the catalyst.

References

[1] San Martín Rueda, A. (2022), "Cobalt-based catalysts for advanced biofuels synthesis via the Fischer-Tropsch process".

[2] IEA (2022), World Energy Outlook 2022, IEA, Paris. Obtained from: https://www.iea.org/reports/world-energy-outlook-2022 (11/04/2023), License: CC BY 4.0 (report); CC BY NC SA 4.0 (Annex A)

[3] Ail, S. S., & Dasappa, S. (2016). Biomass to liquid transportation fuel via Fischer Tropsch synthesis–Technology review and current scenario. *Renewable and sustainable energy reviews*, *58*, 267-286.

[4] Gholami, Z., Tišler, Z., & Rubáš, V. (2021). Recent advances in Fischer-Tropsch synthesis using cobalt-based catalysts: A review on supports, promoters, and reactors. *Catalysis Reviews*, *63*(3), 512-595.

[5] Torres Galvis, H. M., & de Jong, K. P. (2013). Catalysts for production of lower olefins from synthesis gas: a review. *ACS catalysis*, *3*(9), 2130-2149.

[6] Woolcock, P. J., & Brown, R. C. (2013). A review of cleaning technologies for biomass-derived syngas. *Biomass and bioenergy*, *52*, 54-84.

[7] Bartholomew, C. H. (2001). Mechanisms of catalyst deactivation. *Applied Catalysis A: General*, *212*(1-2), 17-60.

[8] Hamelinck, C. N., Faaij, A. P., den Uil, H., & Boerrigter, H. (2004). Production of FT transportation fuels from biomass; technical options, process analysis and optimisation, and development potential. *Energy*, *29*(11), 1743-1771.

[9] dos Santos, R. G., & Alencar, A. C. (2020). Biomass-derived syngas production via gasification process and its catalytic conversion into fuels by Fischer Tropsch synthesis: A review. *International Journal of Hydrogen Energy*, *45*(36), 18114-18132.

[10] van Steen, E., & Claeys, M. (2008). Fischer-Tropsch catalysts for the biomass-to-liquid (BTL)-process. *Chemical Engineering & Technology: Industrial Chemistry-Plant Equipment-Process Engineering-Biotechnology*, *31*(5), 655-666.

[11] Balonek, C. M., Lillebø, A. H., Rane, S., Rytter, E., Schmidt, L. D., & Holmen, A. (2010). Effect of alkali metal impurities on Co–Re catalysts for Fischer–Tropsch synthesis from biomass-derived syngas. *Catalysis letters*, *138*, 8-13.

[12] Gavrilović, L., Brandin, J., Holmen, A., Venvik, H. J., Myrstad, R., & Blekkan, E. A. (2018). Deactivation of co-based Fischer–Tropsch catalyst by aerosol deposition of potassium salts. *Industrial & Engineering Chemistry Research*, *57*(6), 1935-1942.

[13] Mahmoudi, H., Mahmoudi, M., Doustdar, O., Jahangiri, H., Tsolakis, A., Gu, S., & LechWyszynski, M. (2017). A review of Fischer Tropsch synthesis process, mechanism, surface chemistry and catalyst formulation. *Biofuels Engineering*, *2*(1), 11-31.

[14] Molino, A., Larocca, V., Chianese, S., & Musmarra, D. (2018). Biofuels production by biomass gasification: A review. *Energies*, *11*(4), 811.

[15] De Blasio, C., & De Blasio, C. (2019). Fischer–Tropsch (FT) synthesis to biofuels (BtL process). *Fundamentals of Biofuels Engineering and Technology*, 287-306.

[16] Lillebø, A. H., Patanou, E., Yang, J., Blekkan, E. A., & Holmen, A. (2013). The effect of alkali and alkaline earth elements on cobalt based Fischer–Tropsch catalysts. *Catalysis Today*, *215*, 60-66.

[17] Boerrigter, H. P. C. H., Calis, H. P., Slort, D. J., Bodenstaff, H., Kaandorp, A. J., Den Uil, H., ... & Veringa, H. J. (2004). Gas cleaning for integrated biomass gasification (BG) and Fischer-Tropsch (FT) systems. *Energy research Centre of the Netherlands (ECN), Petten, The Netherlands, report C--04-056*.

[18] Visconti, C. G., Lietti, L., Forzatti, P., & Zennaro, R. (2007). Fischer–Tropsch synthesis on sulphur poisoned Co/Al_2O_3 catalyst. *Applied Catalysis A: General*, *330*, 49-56.

[19] Borg, Ø., Hammer, N., Enger, B. C., Myrstad, R., Lindvåg, O. A., Eri, S., ... & Rytter, E. (2011). Effect of biomass-derived synthesis gas impurity elements on cobalt Fischer–Tropsch catalyst performance including in situ sulphur and nitrogen addition. *Journal of Catalysis*, *279*(1), 163-173.

[20] Ma, W., Jacobs, G., Pendyala, V. R. R., Sparks, D. E., Shafer, W. D., Thomas, G. A., ... & Davis, B. H. (2018). Fischer-Tropsch synthesis. Effect of KCl contaminant on the performance of iron and cobalt catalysts. *Catalysis Today*, *299*, 28-36.

[21] Glazer, M. P., Khan, N. A., de Jong, W., Spliethoff, H., Schürmann, H., & Monkhouse, P. (2005). Alkali metals in circulating fluidized bed combustion of biomass and coal: measurements and chemical equilibrium analysis. *Energy & fuels*, *19*(5), 1889-1897.

[22] Gnanamani, M. K., Pendyala, V. R. R., Jacobs, G., Sparks, D. E., Shafer, W. D., & Davis, B. H. (2014). Fischer–Tropsch synthesis: Effect of halides and potassium addition on activity and selectivity of cobalt. *Catalysis letters*, *144*, 1127-1133.

[23] Froment, K., Defoort, F., Bertrand, C., Seiler, J. M., Berjonneau, J., & Poirier, J. (2013). Thermodynamic equilibrium calculations of the volatilization and condensation of inorganics during wood gasification. *Fuel*, *107*, 269-281.

[24] Westberg, H. M., Byström, M., & Leckner, B. (2003). Distribution of potassium, chlorine, and sulfur between solid and vapor phases during combustion of wood chips and coal. *Energy & Fuels*, *17*(1), 18-28.

[25] Kling, Å., Andersson, C., Myringer, Å., Eskilsson, D., & Järås, S. G. (2007). Alkali deactivation of high-dust SCR catalysts used for NOx reduction exposed to flue gas from 100 MW-scale biofuel and peat fired boilers: Influence of flue gas composition. *Applied Catalysis B: Environmental*, *69*(3-4), 240-251.

[26] Gavrilović, L., Brandin, J., Holmen, A., Venvik, H. J., Myrstad, R., & Blekkan, E. A. (2018). Fischer-Tropsch synthesis—Investigation of the deactivation of a Co catalyst by exposure to aerosol particles of potassium salt. *Applied Catalysis B: Environmental*, *230*, 203-209.

[27] Leibold, H., Hornung, A., & Seifert, H. (2008). HTHP syngas cleaning concept of two stage biomass gasification for FT synthesis. *Powder Technology*, *180*(1-2), 265-270.

[28] Tijmensen, M. J., Faaij, A. P., Hamelinck, C. N., & van Hardeveld, M. R. (2002). Exploration of the possibilities for production of Fischer Tropsch liquids and power via biomass gasification. *Biomass and bioenergy*, *23*(2), 129-152.

[29] Sikarwar, V. S., Zhao, M., Fennell, P. S., Shah, N., & Anthony, E. J. (2017). Progress in biofuel production from gasification. *Progress in Energy and Combustion Science*, *61*, 189-248.

[30] Göransson, K., Söderlind, U., He, J., & Zhang, W. (2011). Review of syngas production via biomass DFBGs. *Renewable and Sustainable Energy Reviews*, *15*(1), 482-492.

[31] Teimouri, Z., Abatzoglou, N., & Dalai, A. K. (2021). Kinetics and selectivity study of Fischer–Tropsch synthesis to C_{5+} hydrocarbons: a review. *Catalysts*, *11*(3), 330.

[32] Amghizar, I., Vandewalle, L. A., Van Geem, K. M., & Marin, G. B. (2017). New trends in olefin production. *Engineering*, *3*(2), 171-178.

[33] ChemAnalyst (2023), Ethylene Market Analysis. Obtained from: https://www.chemanalyst.com/industry-report/ethylene-market-638 (11/04/2023)

[34] Yahyazadeh, A., Dalai, A. K., Ma, W., & Zhang, L. (2021). Fischer–Tropsch synthesis for light olefins from syngas: a review of catalyst development. *Reactions*, *2*(3), 227-257.

[35] Van de Loosdrecht, J., Botes, F. G., Ciobica, I. M., Ferreira, A. C., Gibson, P., Moodley, D. J., & Niemantsverdriet, J. W. (2013). Fischer-Tropsch synthesis: catalysts and chemistry. *Surface Inorganic Chemistry and Heterogeneous Catalysis*, *7*.

[36] Moulijn, J. A., Makkee, M., & Van Diepen, A. E. (2013). *Chemical process technology*. John Wiley & Sons.

[37] Corral Valero, M., & Raybaud, P. (2013). Cobalt catalyzed Fischer–Tropsch synthesis: perspectives opened by first principles calculations. *Catalysis letters*, *143*, 1-17.

[38] Niemantsverdriet, J. W., & Chorkendorff, I. (2006). *Concepts of modern catalysis and kinetics*. John Wiley & Sons.

[39] Cheng, J., Hu, P., Ellis, P., French, S., Kelly, G., & Lok, C. M. (2010). Some understanding of Fischer–Tropsch synthesis from density functional theory calculations. *Topics in Catalysis*, *53*, 326-337.

[40] Agrawal, R., Phatak, P., & Spanu, L. (2018). Effect of phase and size on surface sites in cobalt nanoparticles. *Catalysis Today*, *312*, 174-180.

[41] van Santen, R. A., Ghouri, M. M., Shetty, S., & Hensen, E. M. (2011). Structure sensitivity of the Fischer–Tropsch reaction; molecular kinetics simulations. *Catalysis Science & Technology*, *1*(6), 891-911.

[42] Fischer, N., Van Steen, E., & Claeys, M. (2013). Structure sensitivity of the Fischer–Tropsch activity and selectivity on alumina supported cobalt catalysts. *Journal of Catalysis*, *299*, 67-80.

[43] van Helden, P., Ciobîcă, I. M., & Coetzer, R. L. (2016). The size-dependent site composition of FCC cobalt nanocrystals. *Catalysis Today*, *261*, 48-59.

[44] Borg, Ø., Eri, S., Blekkan, E. A., Storsæter, S., Wigum, H., Rytter, E., & Holmen, A. (2007). Fischer–Tropsch synthesis over γ-alumina-supported cobalt catalysts: Effect of support variables. *Journal of Catalysis*, *248*(1), 89-100.

[45] Jacobs, G., Das, T. K., Zhang, Y., Li, J., Racoillet, G., & Davis, B. H. (2002). Fischer–Tropsch synthesis: support, loading, and promoter effects on the reducibility of cobalt catalysts. *Applied Catalysis A: General*, *233*(1-2), 263-281.

[46] Morales, F., & Weckhuysen, B. M. (2006). Promotion effects in Co-based Fischer–Tropsch catalysis. *Catalysis*, *19*, 1-40.

[47] Hu, J., Yu, F., & Lu, Y. (2012). Application of Fischer–Tropsch synthesis in biomass to liquid conversion. *Catalysts*, *2*(2), 303-326.

[48] Pedersen, E. Ø., Svenum, I. H., & Blekkan, E. A. (2018). Mn promoted Co catalysts for Fischer-Tropsch production of light olefins–An experimental and theoretical study. *Journal of Catalysis*, *361*, 23-32.

[49] Pedersen, E. Ø., & Blekkan, E. A. (2018). Noble Metal Promoted CoMn Catalysts for Fischer–Tropsch Synthesis. *Catalysis Letters*, *148*, 1027-1034.

[50] Johnson, G. R., Werner, S., & Bell, A. T. (2015). An investigation into the effects of Mn promotion on the activity and selectivity of Co/SiO_2 for Fischer–Tropsch synthesis: evidence for enhanced CO adsorption and dissociation. *ACS Catalysis*, *5*(10), 5888-5903.

[51] Cano, F. M., Gijzeman, O. L. J., De Groot, F. M. F., & Weckhuysen, B. M. (2004). Manganese promotion in cobalt-based Fischer-Tropsch catalysis. In *Studies in surface science and catalysis* (Vol. 147, pp. 271-276). Elsevier.

[52] Tsakoumis, N. E., Rønning, M., Borg, Ø., Rytter, E., & Holmen, A. (2010). Deactivation of cobalt based Fischer–Tropsch catalysts: A review. *Catalysis Today*, *154*(3-4), 162-182.

[53] Moodley, D. J. (2008). On the deactivation of cobalt-based Fischer-Tropsch synthesis catalysts. *American Chemical Society, Division of Petrochemical Chemistry*, *53*, 122-125.

[54] Gavrilović, L., Save, J., & Blekkan, E. A. (2019). The effect of potassium on cobalt-based Fischer–Tropsch catalysts with different cobalt particle sizes. *Catalysts*, *9*(4), 351.

[55] Gaube, J., & Klein, H. F. (2008). The promoter effect of alkali in Fischer-Tropsch iron and cobalt catalysts. *Applied Catalysis A: General*, *350*(1), 126-132.

[56] Pansare, S. S., & Allison, J. D. (2010). An investigation of the effect of ultra-low concentrations of sulfur on a Co/γ-Al_2O_3 Fischer–Tropsch synthesis catalyst. *Applied Catalysis A: General*, *387*(1-2), 224-230.

[57] Sparks, D. E., Jacobs, G., Gnanamani, M. K., Pendyala, V. R. R., Ma, W., Kang, J., ... & Davis, B. H. (2013). Poisoning of cobalt catalyst used for Fischer–Tropsch synthesis. *Catalysis today*, *215*, 67-72.

[58] Storsæter, S., Borg, Ø., Blekkan, E. A., & Holmen, A. (2005). Study of the effect of water on Fischer–Tropsch synthesis over supported cobalt catalysts. *Journal of Catalysis*, *231*(2), 405-419.

[59] Dalai, A. K., & Davis, B. H. (2008). Fischer–Tropsch synthesis: a review of water effects on the performances of unsupported and supported Co catalysts. *Applied Catalysis A: General*, *348*(1), 1-15.

[60] Krishnamoorthy, S., Tu, M., Ojeda, M. P., Pinna, D., & Iglesia, E. (2002). An investigation of the effects of water on rate and selectivity for the Fischer–Tropsch synthesis on cobalt-based catalysts. *Journal of Catalysis*, *211*(2), 422-433.

[61] Fratalocchi, L., Visconti, C. G., Lietti, L., Groppi, G., Tronconi, E., Roccaro, E., & Zennaro, R. (2016). On the performance of a Co-based catalyst supported on modified γ-Al 2 O 3 during Fischer–Tropsch synthesis in the presence of co-fed water. *Catalysis Science & Technology*, *6*(16), 6431-6440.

[62] Okoye-Chine, C. G., Moyo, M., Liu, X., & Hildebrandt, D. (2019). A critical review of the impact of water on cobalt-based catalysts in Fischer-Tropsch synthesis. *Fuel Processing Technology*, *192*, 105-129.

[63] Ma, Z., & Zaera, F. (2006). Characterization of heterogeneous catalysts. *Surface and Nanomolecular Catalysis*, 1-37.

[64] Ertl, G., Knözinger, H., & Weitkamp, J. (Eds.). (1997). *Handbook of heterogeneous catalysis* (Vol. 2, pp. 427-440). Weinheim: VCH.

[65] Jones, R. D., & Bartholomew, C. H. (1988). Improved flow technique for measurement of hydrogen chemisorption on metal catalysts. *Applied Catalysis*, *39*, 77-88.

[66] Pendyala, V. R. R., Gnanamani, M. K., Jacobs, G., Ma, W., Shafer, W. D., & Davis, B. H. (2013). Fischer–Tropsch synthesis: effect of ammonia impurities in syngas feed over a cobalt/alumina catalyst. *Applied Catalysis A: General*, *468*, 38-43.

[67] HURST, Nicholas W., et al. Temperature programmed reduction. *Catalysis Reviews Science and Engineering*, 1982, vol. 24, no 2, p. 233-309.

[68] Beckhoff, B., Kanngießer, B., Langhoff, N., Wedell, R., & Wolff, H. (Eds.). (2007). *Handbook of practical X-ray fluorescence analysis*. Springer Science & Business Media.

[69] Muller, D. A. (2009). Structure and bonding at the atomic scale by scanning transmission electron microscopy. *Nature materials*, *8*(4), 263-270.

[70] Kapteijn, F., Vanlangeveld, A. D., Moulijn, J. A., Andreini, A., Vuurman, M. A., Turek, A. M., ... & Wachs, I. E. (1994). Alumina-supported manganese oxide catalysts: I. Characterization: effect of precursor and loading. *Journal of Catalysis*, *150*(1), 94-104.

[71] López-Bascón, M. A., & De Castro, M. L. (2020). Soxhlet extraction. In *Liquid-phase extraction* (pp. 327-354). Elsevier.

[72] Borg, Ø., Hammer, N., Eri, S., Lindvåg, O. A., Myrstad, R., Blekkan, E. A., ... & Holmen, A. (2009). Fischer–Tropsch synthesis over un-promoted and Re-promoted γ-Al_2O_3 supported cobalt catalysts with different pore sizes. *Catalysis Today*, *142*(1-2), 70-77.

[73] Van de Loosdrecht, J., Balzhinimaev, B., Dalmon, J. A., Niemantsverdriet, J. W., Tsybulya, S. V., Saib, A. M., ... & Visagie, J. L. (2007). Cobalt Fischer-Tropsch synthesis: deactivation by oxidation?. *Catalysis Today*, *123*(1-4), 293-302.

[74] Fischer, N., Clapham, B., Feltes, T., & Claeys, M. (2015). Cobalt-based Fischer–Tropsch activity and selectivity as a function of crystallite size and water partial pressure. *Acs Catalysis*, *5*(1), 113-121.

[75] Oton, L. F., Oliveira, A. C., de Araujo, J. C., Araujo, R. S., de Sousa, F. F., Saraiva, G. D., ... & Campos, A. (2020). Selective catalytic reduction of NOx by CO (CO-SCR) over metal-supported nanoparticles dispersed on porous alumina. *Advanced Powder Technology*, *31*(1), 464-476.

[76] Chen, Q., Svenum, I. H., Gavrilovic, L., Chen, D., & Blekkan, E. A. (2019). Effect of trace potassium on hydrogen adsorption and dissociation on hcp cobalt: A density functional theory study. *Surface Science*, *681*, 24-31.

[77] Storsæter, S., Borg, Ø., Blekkan, E. A., Tøtdal, B., & Holmen, A. (2005). Fischer–Tropsch synthesis over Re-promoted Co supported on Al_2O_3, SiO_2 and TiO_2: effect of water. *Catalysis today*, *100*(3-4), 343-347.

[78] Saib, A. M., Moodley, D. J., Ciobîcă, I. M., Hauman, M. M., Sigwebela, B. H., Weststrate, C. J., ... & Van de Loosdrecht, J. (2010). Fundamental understanding of deactivation and regeneration of cobalt Fischer–Tropsch synthesis catalysts. *Catalysis Today*, *154*(3-4), 271-282.

[79] Argyle, M. D., & Bartholomew, C. H. (2015). Heterogeneous catalyst deactivation and regeneration: a review. *Catalysts*, *5*(1), 145-269.

[80] Osman, A. I., Mehta, N., Elgarahy, A. M., Al-Hinai, A., Al-Muhtaseb, A. A. H., & Rooney, D. W. (2021). Conversion of biomass to biofuels and life cycle assessment: a review. *Environmental Chemistry Letters*, *19*(6), 4075-4118.

[81] Moulijn, J. A., Makkee, M., & Van Diepen, A. E. (2013). *Chemical process technology*. John Wiley & Sons.

Appendix

A Synthesis Calculations

The following Table A1 shows the amount of the salts used during the catalyst synthesis. All of them were dissolved in deionized water.

Table A1. Amount of the Mn, Co and Re-compounds for catalyst synthesis

Catalyst	Support (g)	Mn		Co		Re	
		%	$Mn(NO_3)_2{\cdot}4H_2O$ (g)	%	$Co(NO_2)_2{\cdot}6H_2O$ (g)	%	$HReO_4$ (mL)
$CoReMn/Al_2O_3$	12.5	3.75	2.27	15	11.36	0.05	0.06
$10CoReMn/Al_2O_3$	12.5	3.75	2.27	10	7.10	0.05	0.05
$CoReMn/SiO_2$	7.5	3.75	1.36	15	6.98	0.05	0.03
$CoReMn/TiO_2$	20.0	3.75	3.64	15	18.63	0.05	0.09

The amounts of the Mn, Co and Re compounds were calculated by Equation A.1, where $m_{compound}$ refers to mass of $Mn(NO_3)_2{\cdot}4H_2O$, $Co(NO_2)_2{\cdot}6H_2O$ and $HReO_4$, M_{melem} is the molecular mass of the element (Mn,Co,Re) and m_{elem} refers to the mass of Mn, Co and Re impregnated in the support, whose value was determined by Equation A.2.

$$m_{compound} = \frac{M_{m_{salt}}}{M_{m_{elem}}} \cdot m_{elem} \tag{A.1}$$

$$m_{elem} = \frac{m_{support} \cdot \%\ \text{elem}}{1 - \text{F} \cdot \%\ \text{elem}} \tag{A.2}$$

Regarding the second equation, F represents a factor that takes into account the molar masses of the constituents. Since the compounds will be in oxide form in the catalyst, it is necessary to perform some initial calculations to determine this factor (Equation A.3). Mm_{oxide} represents the molecular mass of the oxide (MnO_2, CO_3O_4, ReO_2) and N is the number of atoms of the element in the oxide. The factor for manganese oxide and the amount of Mn-salt are determined as an example, but same procedure is followed for $Co(NO_2)_2{\cdot}6H_2O$ and $HReO_4$.

$$F = \frac{M_{m_{oxide}}}{N \cdot M_{m_{elem}}} \quad \text{(A.3)}$$

$$F_{MnO_2} = \frac{89.94\ g/mol}{1 \cdot 54.94\ g/mol} = 1{,}58$$

$$m_{Mn(NO_3)_2 \cdot 4H_2O} = \frac{M_{m_{Mn(NO_3)_2 \cdot 4H_2O}}}{M_{m_{Mn}}} \cdot \frac{m_{Al_2O_3} \cdot \%\ \mathrm{Mn}}{1 - F_{MnO_2} \cdot \%\ \mathrm{Mn}} = \frac{251.01}{54.94} \cdot \frac{12.5 \cdot 0.0375}{1 - 1.58 \cdot 0.0375}$$

$$m_{Mn(NO_3)_2 \cdot 4H_2O} = 2.27\ g$$

Molecular masses of the involved compounds and factors F derived for the manganese, cobalt, and rhenium oxides are shown in Table A2.

Table A2. Molecular masses of each element and compound and relation between oxides and element molecular masses

Compound	**M_m (g/mol)**	**Factor (F)**
Co	58.93	-
Mn	54.94	-
Re	186.21	-
$Co(NO_2)_2 \cdot 6H_2O$	291.03	-
$Mn(NO_3)_2 \cdot 4H_2O$	251.01	-
$HReO_4$	251.21	-
Co_3O_4	240.80	1.36
MnO_2	86.94	1.58
ReO_2	218.21	1.17
H_2O	18.01	-

Finally, the quantity of deionized water required for dissolution can be determined using equation A.4

$$V_{DI} = m_{sup} \cdot V_{pore} - V_{H_2O} \quad \text{(A.4)}$$

V_{DI} is the necessary amount of deionized water and V_{H2O} the amount of water contributed by the precursor, while V_{pore} refers to the pore volume of the support.

B Additional Results

Figure B1 shows the first set of experiments, where CoReMn/Al_2O_3 is tested with KNO_3, KOH, KCl and K_2SO_4. Solutions of 500 ppm concentration are added after 8 hours and 5000 ppm after 24 hours. The progressive decrease in the initial activity suggests the cross-contamination between experiments.

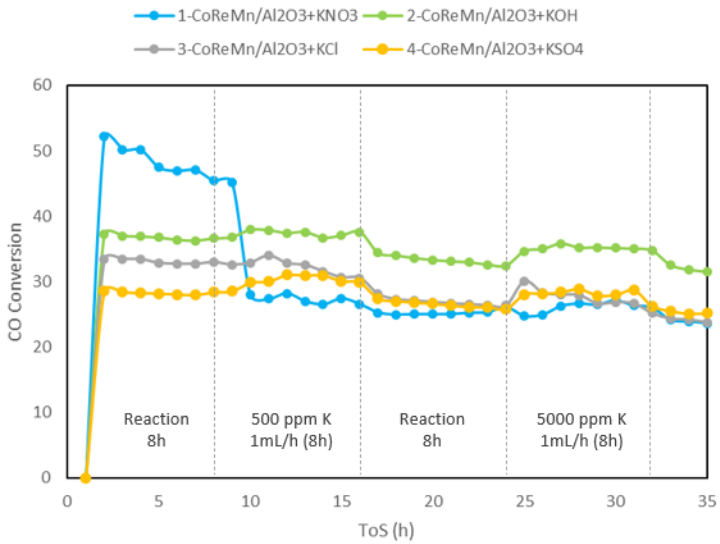

Figure B1. Activity in terms of CO conversion at 240 °C, 5 bar, 15 L/g_{cat}·h of CoReMn/Al_2O_3 posioned with KNO_3, KOH, KCl and K_2SO_4 (additions at 1 mL/h)

Selectivity towards CH_4, C_{5+} products, CO_2 and C_{2-4} olefins on the CoReMn/Al_2O_3 catalyst when poisoned with KCl in two different ways is represented in Figure B2. The blue graph represents the experiment carried out with 70 ppm of solution after 8 hours and 700 ppm after 24 hours. The red graph represents the experiment in which 700 ppm of potassium solution was added after 8 hours of reaction. No great differences are observed. The possible fluctuations in the graph are due to electrical problems in the GC used for the analysis, but it is useful to know the selectivity tendency.

Selectivity towards CH_4, C_{5+} products, CO_2 and C_{2-4} olefins on CoReMn/Al_2O_3, CoReMn/SiO_2 and CoReMn/TiO_2 catalyst when poisoned with KNO_3 compared to the normal activity of the catalyst when is not poisoned is shown in Figures B3-5. Clear differences when potassium is added are observed. Again, the possible fluctuations in the graph are due to electrical problems in the GC used for the analysis, but it is useful to observe the tendency.

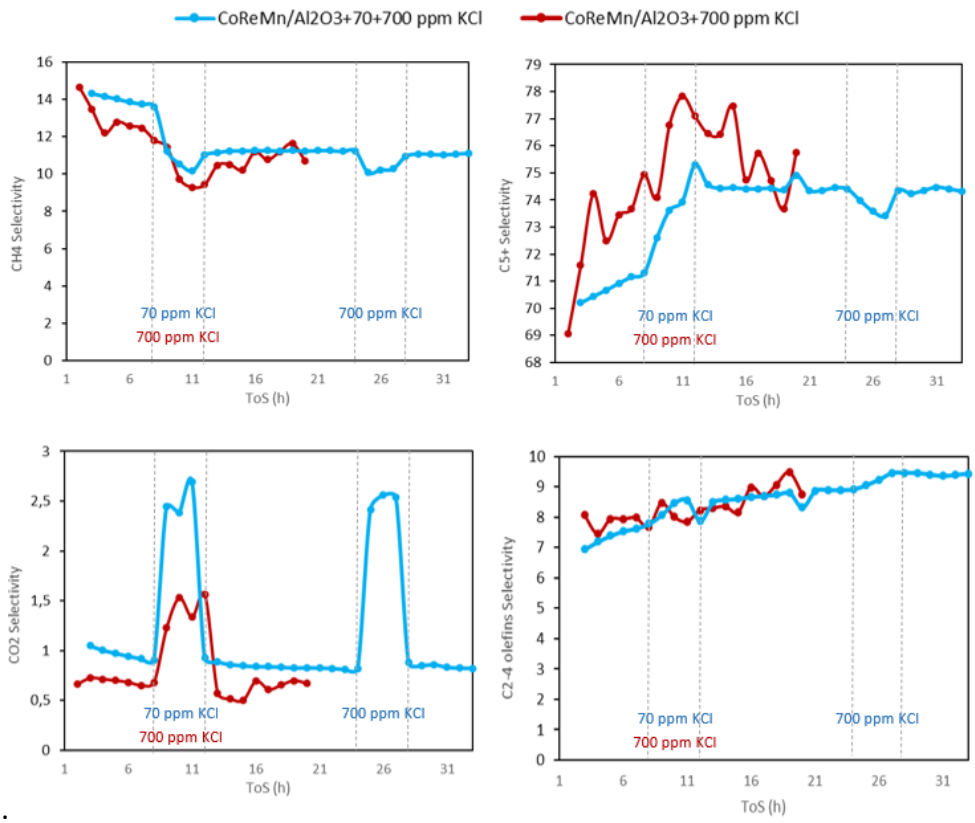

Figure B2. CoReMn/Al_2O_3 selectivity at 240 °C, 5 bar, 15 L/g_{cat}·h towards (1) CH_4, (2) C_{5+} products, (3) CO_2 and (4) C_{2-4} olefins when poisoned with different concentrations of KCl (additions at 2 mL/h)

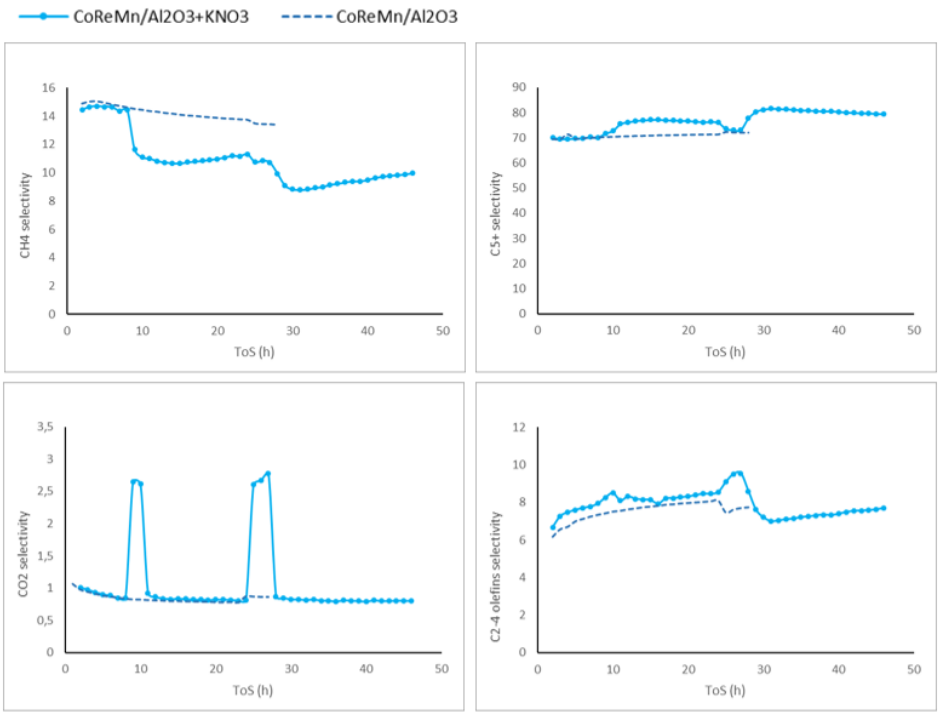

Figure B3. CoReMn/Al_2O_3 selectivity at 240 °C, 5 bar, 15 L/g_{cat}·h towards (1) CH_4, (2) C_{5+} products, (3) CO_2 and (4) C_{2-4} olefins when poisoned with KNO_3 and with normal operation

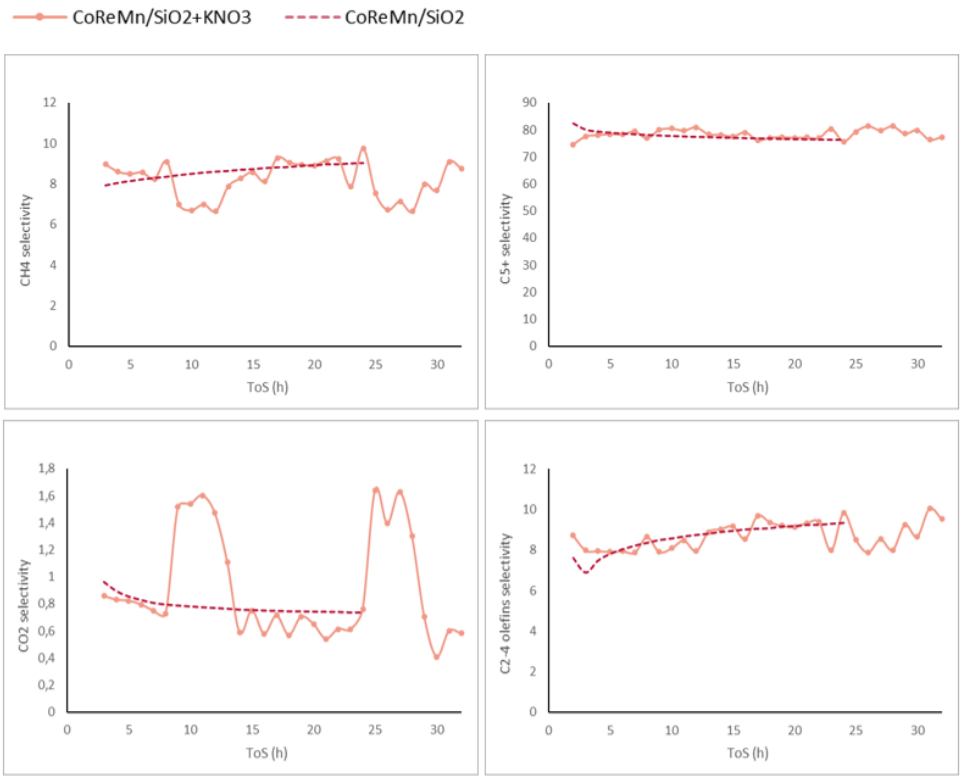

Figure B4. CoReMn/SiO_2 selectivity at 240 °C, 5 bar, 15 L/g_{cat}·h towards (1) CH_4, (2) C_{5+} products, (3) CO_2 and (4) C_{2-4} olefins when poisoned with KNO_3 and with normal operation

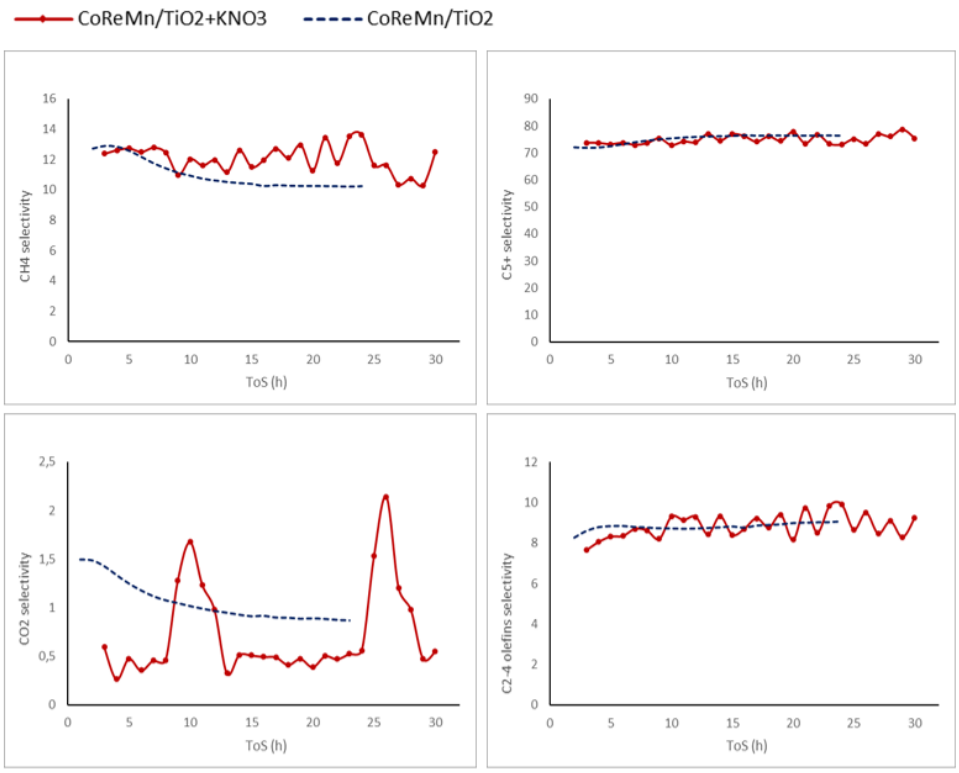

Figure B5. CoReMn/TiO_2 selectivity at 240 °C, 5 bar, 15 L/g_{cat}·h towards (1) CH_4, (2) C_{5+} products, (3) CO_2 and (4) C_{2-4} olefins when poisoned with KNO_3 and with normal operation

The XRD diffractograms of the waxes obtained after reaction with CoReMn/Al_2O_3 when poisoned with KNO_3, KCl and K_2SO_4 are shown in Figure B6. The profiles are also being compared with the XRD diffractograms of the spent catalysts. The results are not consistent enough to confirm that the signal appearing around 21° is due to these waxes.

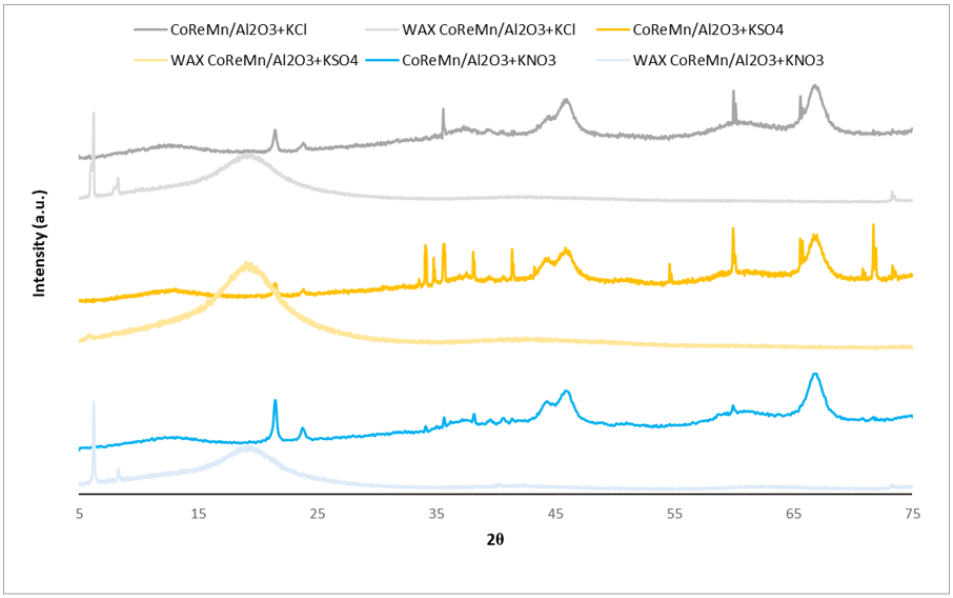

Figura B6. XRD diffractograms of CoReMn/Al_2O_3 and the waxes obtained after its reaction when poisoned with KNO_3, KCl and K_2SO_4

Table B1 below shows the results obtained by XRF for CoReMn/Al_2O_3 before the FT reaction and after the reaction once it is dewaxed. The experiments were performed by Oscar Ivanez, Department of Chemical Engineering, NTNU.

Table B1. Elemental composition by XRF in fresh CoReMn/Al_2O_3 catalyst compared with CoReMn/Al_2O_3 poisoned by KNO_3 and dewaxed

Compound	**Fresh CoReMn/Al_2O_3 catalyst**		**Dewaxed CoReMn/Al_2O_3 poisoned by KNO_3**	
	1st Test	**2nd Test**	**1st Test**	**2nd Test**
Al_2O_3	75.68	76.66	66.02	66.79
K_2O	0.15	0.11	0.41	0.38
MnO_2	10.22	9.97	9.19	9.13
Co_3O_4	12.94	11.37	20.79	20.14
ReO_2	1.99	1.87	3.58	3.54

For each catalyst two different tests were performed. In both cases it was possible to identify the support phases, promoters, and precursors. K_2O could be identified, and it is observed that its content increases once the catalyst is poisoned with KNO_3, so it can be assumed that potassium reached the catalyst bed.

The results obtained after N_2 Adsorption-Desorption on the $CoReMn/Al_2O_3$ catalyst after dewaxing are given by Table B2 and Figure B7). Next, Table B3 and Figure B8 show the results after the H_2 chemisorption performance.

Table B2. Surface area, pore volume and pore size of $CoReMn/Al_2O_3$ posioned with KNO_3 obtained by BET/BJH method and after dewax

Catalyst	Surface area (m^2/g)	Pore volume (cm^3/g)	Pore size (nm)
Al_2O_3	185	0.74	13.4
$CoReMn/Al_2O_3$ Fresh	152	0.53	11.6
$CoReMn/Al_2O_3$ Dewaxed	61	0.20	13.1

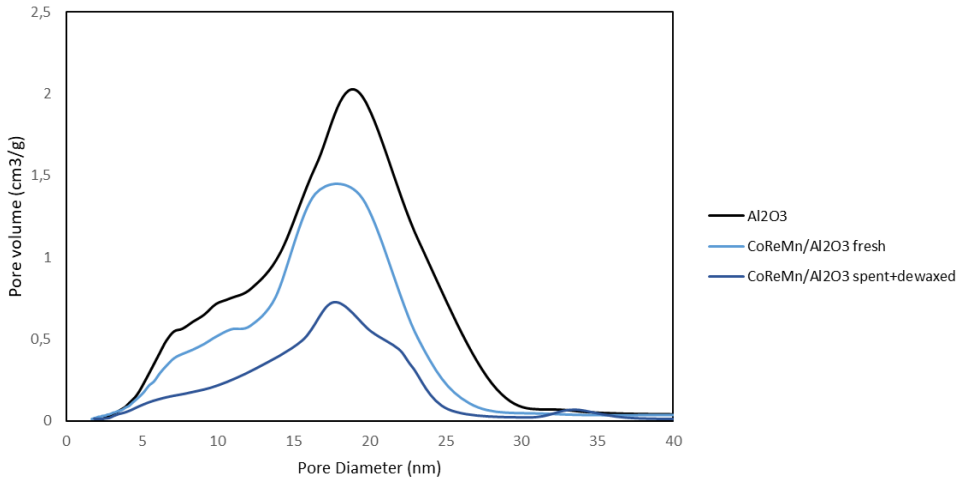

Figure B7. $CoReMn/Al_2O_3$ pore size distribution before and after reaction and dewax

A large drop in both surface area, pore volume and dispersion are observed, as well as an increase in pore size and particle size. However, the results may not be accurate due to the presence of excessive SiC in the catalyst pores and it cannot be confirmed that these changes are due to the addition of potassium.

Table B3. Dispersion and particle size of $CoReMn/Al_2O_3$ before and after reaction and dewaxed obtained by H_2 chemisorption

Catalyst	Dispersion (%)	Particle size (nm)
$CoReMn/Al_2O_3$ Fresh	5.6	17.0
$CoReMn/Al_2O_3$ Dewaxed	2.8	34.6

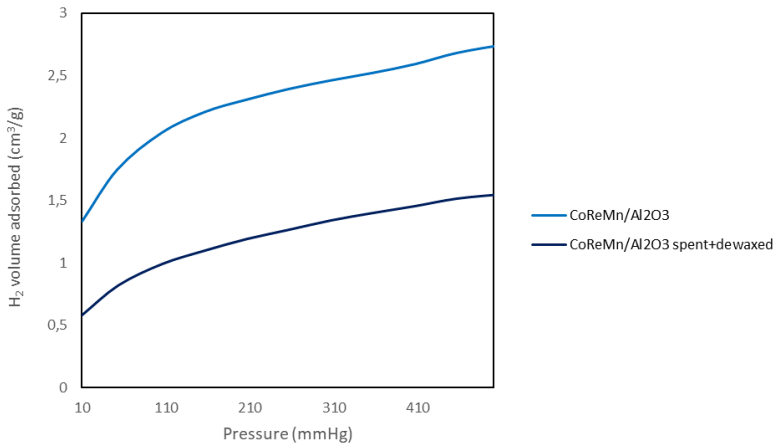

Figure B8. H_2 chemisorption isotherms for $CoReMn/Al_2O_3$ before and after reaction and dewax

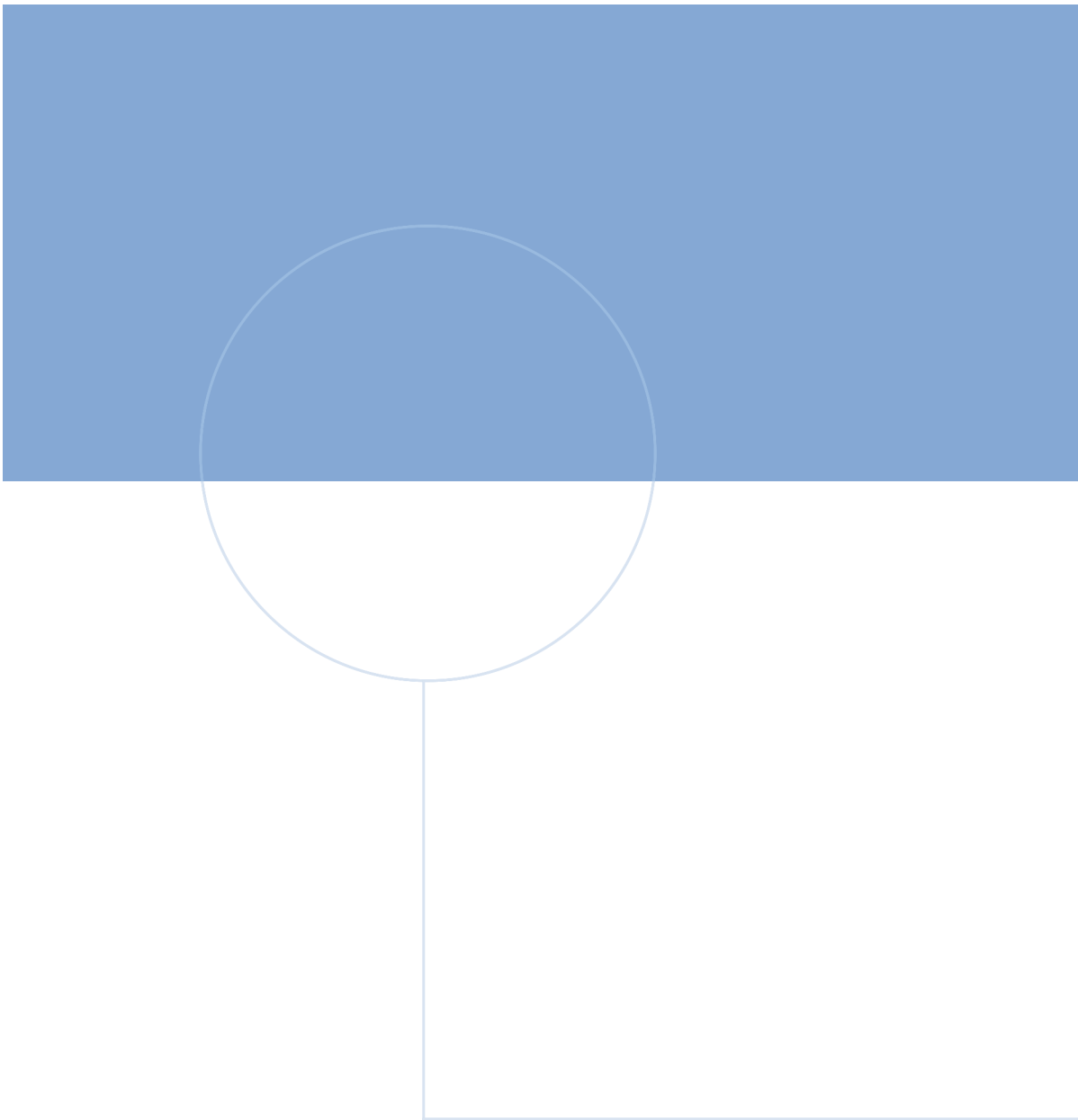

NTNU

Norwegian University of
Science and Technology